Integrated Experimental and Theoretical Investigation of Copper Active Site Properties of a Lytic Polysaccharide Monooxygenase from Serratia marcescens

Alessia Munzone, Manon Pujol, Ashish Tamhankar, Chris Joseph, Ievgen Mazurenko, Marius Réglier, Sergio Jannuzzi, Antoine Royant, Giuseppe Sicoli, Serena Debeer, et al.

To cite this version:

Alessia Munzone, Manon Pujol, Ashish Tamhankar, Chris Joseph, Ievgen Mazurenko, et al.. Integrated Experimental and Theoretical Investigation of Copper Active Site Properties of a Lytic Polysaccharide Monooxygenase from Serratia marcescens. Inorganic Chemistry, 2024, Online ahead of print. 10.1021/acs.inorgchem.4c00602 . hal-04595887

HAL Id: hal-04595887

https://hal.science/hal-04595887v1

Submitted on 31 May 2024

Integrated Experimental and Theoretical Investigation of Copper Active Site Properties of a Lytic Polysaccharide Monooxygenase from *Serratia marcescens*

Alessia Munzone,[a‡§] *Manon Pujol,*[a‡] *Ashish Tamhankar,*[b] *Chris Joseph,*[b] *Ievgen Mazurenko,*[c] *Marius Réglier,*[a] *Sergio A. V. Jannuzzi,*[b] *Antoine Royant,*[d,e] *Giuseppe Sicoli,*[f] *Serena DeBeer,*[b*] *Maylis Orio,*[a*] *A. Jalila Simaan,*[a*] *and Christophe Decroos*[a,g *]

[a] Aix Marseille Univ, CNRS, Centrale Méditerranée, iSm2, 13013 Marseille, France

[b] Max Planck Institute for Chemical Energy Conversion, Stiftstr. 34-36, 45470 Mülheim an der Ruhr, Germany

[c] Aix Marseille Univ, CNRS, BIP UMR 7281, 13009 Marseille, France

[d] Univ. Grenoble Alpes, CNRS, CEA, Institut de Biologie Structurale (IBS), 38000 Grenoble, France

[e] European Synchrotron Radiation Facility, 38043 Grenoble, France

[f] LASIRE UMR CNRS 8516, Université de Lille, 59655 Villeneuve-d'Ascq, France.

[g] Université de Strasbourg, CNRS, INSERM, Institut de Génétique et de Biologie Moléculaire et Cellulaire (IGBMC), Department of Integrative Structural Biology, 67400 Illkirch, France.

KEYWORDS. Lytic polysaccharide monooxygenase, copper metalloenzyme, X-ray crystallography, spectroscopic properties, DFT calculations, redox potential

ABSTRACT. In this paper, we have employed a multidisciplinary approach, combining experimental techniques and density functional theory (DFT) calculations to elucidate key features of the copper coordination environment of the bacterial Lytic Polysaccharide Monooxygenase (LPMO) from *Serratia marcescens* (*Sm*AA10). The structure of the *holo*-enzyme was successfully obtained by X-ray crystallography. We then determined the copper(II) binding affinity using competing ligands and observed that the affinity of the histidine-brace ligands for the copper is significantly higher than previously described. UV-Vis, advanced Electron Paramagnetic Resonance (EPR) and X-ray Absorption Spectroscopy (XAS) techniques, including high energy resolution fluorescence detected (HERFD) XAS, were further used to gain insight into the copper environment both in the Cu(II) and Cu(I) redox states. The experimental data were successfully rationalized by DFT models offering valuable information on the electronic structure and coordination geometry of the copper center. Finally, the Cu(II)/Cu(I) redox potential was determined using two different methods at *ca*. 350 mV *vs*. NHE, and rationalized by DFT calculations. This integrated approach not only advances our knowledge of the active site properties of *Sm*AA10, but also establishes a robust framework for future studies on similar enzymatic systems.

Introduction

Biomass polysaccharides (*e.g.* cellulose or chitin) are abundant biopolymers that are increasingly considered as renewable resources for the production of bio-sourced chemicals or biofuels.[1] Lytic Polysaccharide Monooxygenases (LPMOs) are copper enzymes that were identified in 2010-2011,[2,3] and that boost the depolymerization of recalcitrant polysaccharides through oxidative mechanisms.[4–7] LPMOs catalyze the hydroxylation of an inert C-H bond (at C1 or C4 position) at the glycosidic bond further leading to chain cleavage (Scheme 1). Hydroxylation of the glycosidic bond by LPMOs necessitates an oxygenated co-substrate. The exact nature of this co-substrate is still under debate but recent findings have shown that LPMOs can use hydrogen peroxide to perform catalytic turn-overs.[8,9] It therefore remains unclear whether LPMOs act as peroxygenases (*i.e.* using H_2O_2) or as monooxygenases (*i.e.* using O_2 and electrons).[8–15]

Scheme 1. Hydroxylation of chitin (C1 position) catalyzed by LPMOs leading to chain cleavage.

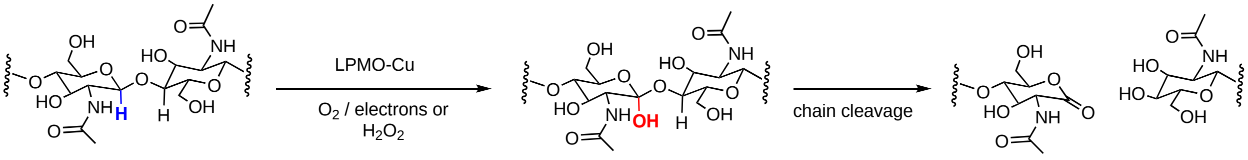

LPMOs are abundantly found in cellulotic or chitinolytic fungi and bacteria, but have also been evidenced in other organisms, such as oomycetes, viruses, plants or insects. Recent findings suggest that they may have wider biological functions beyond the mere oxidation of biopolymers as carbon source for the organisms.[16] LPMOs have been classified into 8 sub-families as "Auxiliary Activity" in the CaZy database (Carbohydrate Active Enzymes, http://www.cazy.org/).[17] Despite low sequence identity across sub-families, LPMOs exhibit a common immunoglobulin-like fold with a solvent-exposed mono-copper active site located on a relatively flat surface that interacts with extended polymeric substrates. The copper center is coordinated by two histidine residues: *(i)* the *N*-terminal histidine bidentately bound *via* the terminal amine and the proximal nitrogen of the imidazole, and *(ii)* the distal nitrogen of the imidazole of the second histidine (Figure 1). This unusual coordination mode has been named "histidine brace" and is found in just a few other cuproproteins such as CopC (a copper transporter),[18] the B site of *p*MMO (particulate methane monooxygenase)[19] or the periplasmic copper-A chaperones (PCuAC) PmoF1 and PmoF2 from methane oxidizing bacteria.[20] Second coordination sphere residues appear to be less conserved than the copper histidine brace motif. In particular, the axial position can be occupied either by a tyrosine or phenylalanine (Figure 1). In AA10 LPMOs, an alanine can be found close to the active site although some variability is also observed at this position.[21] Recent mutations studies highlighted that second sphere residues play an important role in catalytic function.[22]

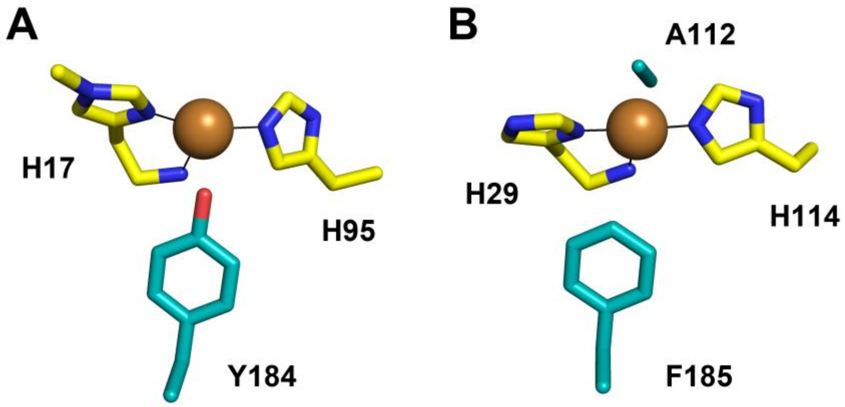

Figure 1. Active sites of typical (**A**) AA9 (PDB entry 4EIS[23]) and (**B**) chitin-active AA10 LPMOs (PDB entry 4ALC[24]) with the histidine brace ligands (C in yellow, N in blue) and the second

coordination sphere residues: the axial tyrosine or phenylananine residues and the alanine in the case of AA10 (C in teal, O in red).

Soon after their recent discovery, LPMOs have been the focus of multidisciplinary and intensive research, notably due to their potential use for biotechnological applications. However, many questions remain unanswered concerning their active site properties and the structural dynamics undergone during redox events and catalysis. One key step towards a better understanding of LPMO's structure-function relationships is to obtain precise structural and spectroscopic data of the active site at both Cu(II) and Cu(I) redox states. Herein, the active site properties of an archetypal chitin-active bacterial enzyme from the AA10 sub-family (one of the most studied together with the AA9 sub-family) have been extensively characterized. We specifically focused on the LPMO from *Serratia marcescens* (*Sm*AA10, initially named CBP21) which was the first evidenced LPMO in 2010.[2] Noteworthy, *Sm*AA10 has emerged as a model enzyme as it is one of the most-studied amongst LPMOs.[2,25–31] Yet, several biophysical data are missing including the crystallographic structure of the Cu-bound enzyme. In the present work, we report the crystal structure of the metalated enzyme as well as a comprehensive study of the active site properties at both Cu(II) and Cu(I) redox states. We have in particular used advanced Electron Paramagnetic Resonance (EPR) techniques, partial fluorescence yield (PFY) and high energy resolution fluorescence detected (HERFD) X-Ray absorption (XAS) spectroscopy.[32,33] The comparison of experimental data with that calculated by Density Functional Theory (DFT) based on structural models of the active site provides robust validation of the structural and electronic description of the active site. Finally, the Cu(II)/Cu(I) redox potential was measured using two different experimental approaches and found at *ca*. 350 mV *vs*. NHE, a value higher than that previously reported.[29] This redox potential value was further supported by DFT calculations. Altogether, this work provides a complete structural and electronic description of the copper active site of *Sm*AA10, a model enzyme from the chitin-active AA10 sub-family. Overall, our integrated approach establishes a robust framework for future studies on LPMOs and copper-containing systems.

Materials and Methods

Gene cloning, protein expression and purification were performed as previously reported[31] and are described in Supplementary Information.

Protein crystallization

Protein crystallization conditions were screened with the commercial kits Index HT, Crystal, and PEG Rx (Hampton Research, USA) using the vapor diffusion method (sitting drops). A 1 µL drop of precipitant was manually added to a 1 µL drop containing 10 or 15 mg/mL Cu(II)-loaded *Sm*AA10 and 500 µM $CuSO_4$ in 50 mM MES (pH 6.5) and equilibrated against an 80 µL reservoir of precipitant solution at 21°C. PEG Rx screen condition C4 (0.1 M citric acid (pH 3.5), 25% w/v PEG 3350) and Crystal screen condition A9 (0.1 M citric acid (pH 5.6), 0.2 M ammonium acetate, 30% w/v PEG 4000) led to initial hits. Optimization of crystallization conditions was further performed by a grid screen with the following precipitant conditions: 0.1 M citric acid (pH 3.2 to 4.0), 20 to 31% w/v PEG 3350. Rod-shaped crystals typically appeared within one to two days.

Crystallographic data collection and structure refinement

Before flash-cooling in liquid nitrogen, crystals were cryoprotected by transfer into a precipitant solution supplemented with 15% v/v glycerol. The best diffracting crystals were obtained for precipitant solutions containing 0.1 M citric acid (pH 3.7), 25% w/v PEG 3350 (for *Sm*AA10 at a concentration of 15 mg/mL). X-ray diffraction data were collected at the European Synchrotron Radiation Facility (ESRF, Grenoble, France) on beamline FIP2-BM07 at 100 K at a wavelength of 0.9795 Å. The autoPROC[34] pipeline chosen from the series of automated reduction pipelines,[35] for which results are available through the web information management system ISPyB[36] was used for data integration and reduction. A molecular replacement solution was determined with PHASER[37] implemented in PHENIX[38] using as a search probe the atomic coordinates (PDB accession code 2BEM) of apo-*Sm*AA10 less ion, and solvent. Iterative cycles of refinement in PHENIX[38] followed by manual model rebuilding in COOT[39] were performed until no further improvement of the refinement statistics. After several rounds of refinement, ions, ligands, and solvent molecules were included in the model. In the final stages, translation libration screw (TLS) refinement was performed. TLS groups were automatically determined using PHENIX.[38] Side chains of residue K197 (monomers A and B) was disordered and thus excluded from the final model. Detailed data collection and refinement statistics are recorded in Table 1.

Table 1. Data collection and refinement statistics

	Wild-type *Sm*AA10
Unit cell	
space group symmetry	*C2*
a, b, c (Å)	53.6, 106.7, 55.5
α, β, γ (deg)	90, 100.0, 90
Data collection	
wavelength (Å)	0.9795
resolution limits (Å)	27.31-1.46
total/unique reflections	182343/52821
R_{merge}[a,b]	0.090 (0.985)
$CC_{1/2}$[a,c]	99.6 (56.7)
I/σ(I)[a]	9.0 (1.1)
redundancy[a]	3.5 (3.3)
completeness (%)[a]	98.4 (96.0)
Refinement	
reflections used in refinement/test set	52791/1998
R_{cryst}[a,d]	0.160 (0.304)
R_{free}[a,e]	0.189 (0.330)
protein atoms[f]	2741
water molecules[f]	402
Cu ions[f]	2
citrate molecules[f]	2
glycerol molecules[f]	2
Rms deviations from ideal geometry	
bonds (Å)	0.004
angles (°)	0.76
Average B factors (Å)	
protein atoms	17.7
water molecules	27.4
ligands	23.5
Ramachandran plot (%)[g]	
favored	98.9
allowed	1.1
outliers	0
PDB accession code	8RRY

[a] Values in parentheses refer to the highest shell of data. [b] $R_{merge} = \sum|I_h - \langle I\rangle_h|/\sum I_h$, where $\langle I\rangle_h$ is the average intensity for reflection *h* calculated from replicate reflections. [c] Pearson correlation coefficient between random half-datasets. [d] $R_{cryst} = \sum||F_o| - |F_c||/\sum|F_o|$ for reflections contained in the working set. $|F_o|$ and $|F_c|$ are the observed and calculated structure factor amplitudes, respectively. [e] $R_{free} = \sum||F_o| - |F_c||/\sum|F_o|$ for reflections contained in the test set held aside during refinement. [f] Per asymmetric unit. [g] Calculated with MolProbity.

UV-VIS and Fluorescence

Fluorescence spectra were recorded on a Horiba Jobin-Yvon Fluoromax-4. UV-Visible spectrum was measured on a VARIAN Cary 60 using a HELLMA 1 cm quartz microcuvette (100 μL). Deconvolution was performed using Fityk 1.3 software.

Binding constant determination

The affinity of Cu(II) for apo-*Sm*AA10 was measured at 25°C using competing ligands and monitoring the fraction of protein bound by tryptophan fluorescence quenching. The measurement was based on the use of competing ligands forming 1:1 complexes with Cu(II). Three ligands were tested and the affinity constants of the different ligands for Cu(II) were derived from the literature (at 25°C and at pH 6.5, with ionic strength of 0.1 M):[40] EDTA (*N*,*N*,*N*′,*N*′-ethylenediamine tetraacetic acid) $\log(\beta_{EDTA}) = 14.9$; EGTA (ethyleneglycol-*O*,*O*′-bis(2-aminoethyl)-*N*,*N*,*N*′,*N*′-tetraacetic acid) $\log(\beta_{EGTA}) = 12.5$ and NTA (nitrilotriacetic acid) $\log(\beta_{NTA}) = 9.8$.

The *apo*-*Sm*AA10 was placed in 20 mM MES buffer set at pH 6.5 in the presence of 50 mM Na_2SO_4 (ionic strength I = 0.1 M). Several solutions were then prepared containing from 0 to 1 equivalent of Cu(II) from a concentrated stock solution of $Cu(NO_3)_2$ in water. After 15 minutes, the competing ligand was added in equimolar concentration as compared with that of the protein. To ensure that the system has reached equilibrium, the same reaction was performed starting from L-Cu(II) solutions followed by the addition of the *apo*-protein to the mixtures. The samples were left to equilibrate 24 hours at 25°C. Fluorescence intensities were recorded using $\lambda ex = 290$ nm (5 nm slit width) and $\lambda em = 340$ nm (5 nm slit width). The fraction of metalated protein was calculated using Eq. 1.[40]

$$[\mathrm{PCu}] = \frac{F_{max} - F}{F_{max} - F_{min}} * C_0 \qquad \text{Eq. 1}$$

With c_0 the protein or ligand total concentration, F the fluorescence intensity of the sample, F_{max} the fluorescence intensity of the *apo*-protein and F_{min} the fluorescence intensity of the fully metalated protein.

The concentration of *holo*-protein was then used to calculate the other concentrations and the dissociation constant (K_D) was derived from Eq. 2:

$$\beta_L K_D = \frac{[LCu]*[P]}{[PCu]*[L]} \qquad \text{Eq. 2}$$

With β_L the affinity constant of the competing ligand.

EPR Techniques

The Echo-Detected Field-Swept spectra (EDFS) have been recorded with an ELEXSYS E-580 spectrometer (Bruker) equipped with a Super-Q FTu bridge for X-band (9 GHz) and Q-band (35 GHz). Samples prepared into aqueous buffers have been transferred into 3 × 4 mm (i.d. × o.d.) quartz tubes (flash-frozen into liquid nitrogen, and rapidly inserted into precooled dielectric resonators, ER 4118X-MD5W X-band and ER 5106QT-2w Q-band). X- and Q-band spectra were acquired at 20 K using a Bruker Cryogen-free (Cold-Edge) cooling system. EDFS were acquired using the pulse sequence: $\pi/2$–τ–π–τ–echo to generate Hahn-echo. Microwave pulse lengths $\tau_{\pi/2}$ = 10-12 ns (Q-band) and $\tau_{\pi/2}$ = 16 ns (X-band) have been used; inter-pulse delays of τ = 172 ns (Q-band) and τ = 136 ns (X-band) have been applied. A two-step phase-cycle has been applied to remove all unwanted echoes. Numerical simulation of the EPR spectra was conducted using the Matlab toolbox Easyspin 5.2.3.[41] Hyperfine sublevel correlation (HYSCORE) experiments have been recorded by setting the magnetic field to the maximum of the EDFS spectra. 4-pulse HYSCORE spectra were acquired at 20 K at X-band frequencies 9.72 GHz) with a pulse length of

16 and 32 ns for π/2 and π, respectively, τ set at 132 ns and a 4-step phase cycle. Data were processed and analyzed using the Matlab plugin HYSCOREAN[41] employing Hamming apodization, zero-filling, 2nd order polynomial background correction. Upon diagonal and anti-diagonal spectral symmetrization, a similar amount of noise for each spectrum has been kept by adjusting the minimum contour level percentage accordingly.

Partial Fluorescence Yield (PFY) XAS data collection and processing

The experimental configuration and parameters used to collect the PFY-XAS data were adapted from a previously reported procedure and is again described here.[22] The Cu K-edge PFY-XAS were collected at Diamond Light Source (DLS; Oxfordshire, UK) (3 GeV, 300 mA) at I20-scanning,[42,43] equipped with a four-bounce Si(111) monochromator, rhodium-coated harmonic rejection mirrors. This configuration provided a flux of ~1×10^{12} photons/sec (when unattenuated) at the sample position. The X-ray beam approximated an un-slitted, focused beam spot size of 0.3×0.4 mm^2 (v × h; full width at half maximum (FWHM)). The sample of *Sm*AA10-Cu(I) in pH 6.5 MES (50 mM) was prepared by reduction of *Sm*AA10-Cu(II) using 50 equivalents excess ascorbic acid under anaerobic conditions, followed by purification by size exclusion chromatography and the addition of saturated glucose solution (30 % v/v) as a glassing agent. Each solution was transferred into a Kapton-windowed Delrin cell and frozen in liquid nitrogen. During measurement, the sample cell was suspended in a top loading exchange gas pulse tube He cryostat maintained at 10 K to minimize photodamage. Scans swept the incident energy from 8859 to 9640 eV, and the incident energy was calibrated by simultaneous measurement of a Cu foil, with the first inflection point of the Cu foil set to 8980.3 eV. Three ionization chambers — one before the sample (I_0), one after the sample (I_t), and one after a reference foil (I_{ref}) — were positioned along the beam path, and fluorescence data from the sample was recorded by a 64-element monolithic

Ge detector. For the fluorescence detector, read-out was performed by an Xspress4 digital pulse processor. Damage assessment was performed prior to the collection of the full spectra via a series of short, low-resolution scans at the near-edge region. Flux was attenuated in order to ensure that each sample spot could survive a 12-minute scan, and full spectra were collected at several fresh sample spots.

The *Demeter* software package was utilized for data processing.[44] Using the *Athena* module, the data were truncated to $k = 12.4$ Å^{-1}, background subtracted and normalized. Before the edge region, a linear regression from 8864 to 8956 eV was used; and a cubic polynomial regression was used for the region after the edge, 9136 to 9545 eV. The data were splined (k range: 0–12.4 Å^{-1}, R-background: 1.0, k-weight: 3). The EXAFS were k^3-weighted (to enhance the impact of high-k data), and Fourier transformed (FT) using a Hanning-windowed k range: 2–12 Å^{-1}. The *Artemis* module was utilized to model and fit the FT-EXAFS equipped with FEFF6 at the back end. The fitting range spanned $R = 1.0$–4.0 Å (non-phase shift corrected), and similar scattering paths were grouped together as degenerate when within the $\Delta R = 0.167$ Å resolution. A single E_0 variable was globally applied for all paths in a given fit, and the amplitude reduction factor (S_0^2) was fixed at 0.9 for all paths. An initial fit was performed using FEFF-calculated paths generated from the geometry optimized structure. Atoms used for the FEFF calculation are shown in Figure [3]. The initial fit locked path distances and allowed σ^2 and E_0 to be fit. Path distances (R) were then iteratively fit to approach a final fit in which all variables R, σ^2, and E_0 could be freely floated. Information about selected fits is shown in Table S8 and Figure S9.

High Energy Resolution Fluorescence Detected (HERFD) XAS data collection and processing

Cu Kα HERFD-XANES data were measured at the ID26 beamline at the European Synchrotron Radiation Facility (ESRF, Grenoble, France) (6 GeV and 200 mA).[45] A Si(311) double crystal monochromator was utilized for upstream energy selection and detection was accomplished using a 1 m radius Johann spectrometer equipped with five Si(444) analyzer crystals and a silicon-drift detector windowed to the Cu Kα region. Measurement of a Cu foil prior to data collection was used to calibrate the incident energy, for which the first inflection point of the Cu foil was set to 8980.3 eV, and the energy of the spectrometer was set to the $K\alpha_1$ maximum. The X-ray beam was slitted to an approximate beam spot size of 0.1×0.2 mm^2 (v × h), providing an unattenuated flux of ~5×10^{13} photons/sec at the sample position. Samples of *Sm*AA10-Cu(I) were prepared as described above. During the measurement, the sample temperature was maintained at 20 K using a side loading He cryostat to minimize photodamage. The data were collected by scanning the incident energy from 8960 to 9080 eV. An additional series of scans ranging from 8900 to 9500 eV were collected and used for edge jump normalization. Prior to the collection of the full spectra, a series of short scans at the near-edge region were collected to assess sample vulnerability to X-ray-induced photodamage. Successful acquisition of undamaged spectra was achieved by optimization of attenuation of the incident beam as scan time 90-second scan, and a translation was made to a fresh sample spot between each scan.

For the Kα HERFD data, background subtraction and normalization of the data were performed on the long-range data (8900 to 9500 eV collection range) using a cubic polynomial regression for the post-edge region of 9186–9500 eV. The high-resolution short-range data (8960 to 9080 eV collection range) were adjusted to overlay against the normalized data.

Redox potential determination

Electrochemical measurements were performed as previously described.[31] To enhance the kinetics of the heterogeneous electron transfer between *Sm*AA10 and the electrode necessary to determine its redox potential, a thin layer configuration and electrode modification by carbon nanotubes were used.[46,47] A pyrolytic graphite electrode (PG) with surface area 0.071 cm^2 was polished with 2400 wet emery paper, sonicated in 30% C_2H_5OH solution, and dried. Then, 7 µL of multiwall carbon nanotubes functionalized with NH_2-groups (CNT-NH_2, Dropsens, Spain) dispersed in NMP (0.1 mg/mL) was drop-cast onto the electrode surface and evaporated under vacuum for 15 min. A thin layer configuration was created by depositing 2 µL of 1 mM protein on the CNT-NH_2 surface and immediately covering the electrode with a 7 kDa dialysis membrane, fixed in place with a rubber O-ring.

Cyclic voltammetry was performed in a 3-electrode electrochemical cell comprising a working electrode (modified PG), a Pt-wire auxiliary electrode (Pt wire) and Hg/Hg_2SO_4 (sat. K_2SO_4) as reference electrode. The cell was controlled by a potentiostat Autolab M101 and Nova 2 software (Autolab Metrohm, Netherlands), kept under nitrogen atmosphere. Scan rates in the range of 200 - 0.05 mV/s were used. All the potentials in the text are referred the normal hydrogen electrode (NHE).

Redox titrations were performed under inert atmosphere and at 25°C. LPMO was placed at 200 µM in MES 20 mM set at pH 6.5 in the presence of 5 µM of the following redox mediators: Ferroin, 1,1-ferrocene dicarboxylic acid, mono carboxylic acid ferrocene and 1,1-ferrocene dimethanol. Potentials were adjusted by adding concentrated solutions of freshly prepared dithionite or potassium hexachloroiridate (K_2IrCl_6) solutions and were measured using an Inlab redox micro electrode from Mettler Toledo. For each potential, an aliquot of the solution was withdrawn and placed in an EPR tube for further Cu(II) quantification by double integration of the EPR derivative signal. For redox titrations, *cw* X-band EPR measurement were acquired at 120 K with a Bruker ELEXSYS and a BVT-3000 temperature controller.

Computational details

All DFT computations were conducted using the ORCA program 5.0.[48,49] Structure optimizations were carried out with the BP86 functional[50,51] and def2-TZVP basis sets[52]. The def2/J auxiliary basis sets were used for the Coulomb fitting.[53] Tight SCF was used as convergence criteria together with increased angular and radial integration grids (Grid4 and IntAcc 6.0, respectively, in Orca convention). Slow SCF was used as convergence setting and the full Fock matrix (DirectResetFreq 1) was recalculated for each SCF step. The steric influence of the protein matrix towards the active site geometry was preserved by applying specific constraints on designated terminal hydrogens and backbone carbons.[54] The enzyme under investigation having its active site solvent exposed, all calculations were performed by invoking the implicit solvation model CPCM[55] ($\varepsilon = 20$, refractive index = 1.33).[56] Using the BP86 functional[50,51] and def2-TZVP basis sets [52], we computed redox potentials from the energy change occurring when the oxidized species is reduced in solution[57] We employed the universal solvation model based on density (SMD)[58] in order to evaluate both electrostatic and nonelectrostatic solvation components of the solvation process. The reported values are relative potentials referenced to standard hydrogen electrode and as such, a 0.630 eV shift was applied to convert the calculated Fc^+/Fc reference into NHE[59] for comparison purpose with experimental data. We performed single-point calculations with the B3PW91 functional[60,61] and def2-TZVP basis sets[52] to obtain electronic structures. EPR calculations, namely *g*-tensors, were obtained from single-point calculations using an adapted version of B3PW91[60,61] incorporating 40% Hartree–Fock exchange.[62] aug-cc-pVTZ-Jmod [63] was used as extended basis set for the copper center while the def2-TZVP basis sets[52] were applied to describe other atoms. Hyperfine tensors as well as nuclear quadrupole couplings were computed from additional single-point calculations employing the B3PW91 functional[60,61] together with the aug-cc-pVTZ-Jmod[63], EPR-II[64] and def2-TZVP basis sets[52] for the copper, nitrogens and other atoms, respectively. UV-vis spectral features were predicted within the TD-DFT framework using the BLYP functional[50,65] and def2- TZVP basis sets[52] Simplified TD-DFT using the TDA[66–70] method was employed to compute electronic transitions. The RI approximation[71] was used in calculating the Coulomb term to increase computational efficiency, and in each case, up to 70 excited states were calculated. X-ray absorption spectra were calculated using TD-DFT following previously established protocols[72–74] with CAM-B3LYP[61,65,75] functional with the Tamm-Dancoff approximation. Scalar relativistic effects were included using ZORA[76] with ZORA-def2-TZVP basis sets.[77] The Autoaux generation procedure was used to assign auxiliary basis for coulomb fitting.[78] The chain of spheres approximation (RIJCOSX)[79] was employed for the RI approximation to the Coulomb integrals in addition to the auxiliary basis. These calculations were conducted using the implicit solvation model CPCM[55] ($\varepsilon = 20$, refractive index = 1.33). The SCF convergence criteria was set with "TightSCF" and "SlowConv" keywords. We plotted the absorption spectra with the orca_mapspc program using 0.96 eV and 2.40 eV broadening with Gaussian line shape to compare with HERFD and PFY experimental data, respectively. We added the contributions from the magnetic dipole, electric quadrupole, and electric dipole to determine the oscillator strength. Molecular orbitals and density difference plots were obtained with the orca_plot program and the Chemcraft program was used for visualization (http://chemcraftprog.com).

Results and Discussion

Structural characterization of *Sm*AA10 copper active site

The structure of *Sm*AA10 was previously described for its *apo* form (with a sodium modeled at the place of copper) by both X-ray crystallography and NMR.[28,29] *Apo Sm*AA10 crystallized in the orthorhombic space group $P2_12_12_1$ with three monomers in its asymmetric unit (PDB code 2BEM),[28] and its X-ray crystal structure was solved at 1.55 Å. Its associated mutant Y54A was also crystallized but in different conditions yielding a new crystal form diffracting at 1.80 Å, in the trigonal space group $P3_121$ with two monomers in the asymmetric unit (PDB code 2BEN). In the wild-type *apo* structure, the histidine brace is preorganized with the two histidine side chains (H28 and H114) interacting through a hydrogen bond (2.9-3.0 Å between H28 Nδ and H114 Nε). Some flexibility is observed for the side chain of H28 moving further away in the crystal structure of *Sm*AA10 Y54A mutant and in the solution structure by NMR (PDB code 2LHS).[29] However, Cα of H28 and H114 remain within a distance of 7.5-8.0 Å in the crystal structures and of 10.0-11.2 Å in the solution structure, indicating that the copper binding site is prearranged within the protein scaffold. Intriguingly, a sodium ion coordinated by the histidine brace was modeled in the active site of monomer C in the wild-type structure. At the time the crystal structure was solved, *Sm*AA10 was not yet described as a copper-dependent LPMO, but as a chitin-binding protein possibly leading to an incorrect assignment of the metal ion. Nonetheless, the exact nature of the bound metal ion in this crystal structure remains unclear given that *Sm*AA10 was not reconstituted with Cu(II). This metal ion could possibly be heavier than sodium but with a lower occupancy. For instance, it is known that *Sm*AA10 can also bind Zn(II), even though less tightly than Cu(II).[29]

We crystallized Cu(II)-loaded *Sm*AA10 in conditions consisting of citrate as buffer (0.1 M, pH 3.2 to 4.0), and PEG 3350 as precipitant (20 to 31% w/v), yielding rod-shaped crystals within one to two days. The structure was solved at 1.46 Å resolution for this new crystal form belonging to the monoclinic space group *C*2 with 2 monomers in the asymmetric unit (Table 1). The overall structure of the two monomers is almost identical with a root-mean-square deviation (rmsd) value of 0.18 Å for 169 aligned Cα atoms (Figure 2A). Likewise, no major structural change is observed compared to the previously reported structure of *Sm*AA10 (PDB code 2BEM)[28] with rmsd values ranging from 0.26 to 0.32 Å for 169 aligned Cα atoms depending on superimposed monomers. Within our structure, active site copper ions display full occupancy in both *Sm*AA10 monomers. The coordination geometry of the histidine brace copper ions is similar to previously characterized chitin-active bacterial LPMOs (Table S1).[80] In monomer A, the active site metal ion has a three-coordinate T-shape geometry, which is consistent with a Cu(I) ion, suggesting that X-rays have reduced the resting state Cu(II) ion over the course of data collection (Figure 2B), as previously described for other LPMOs.[21,24,81,82] In contrast, the copper ion in monomer B is in a mixed Cu(II)/Cu(I) redox state as judged from active site geometry and ligand occupancy. Even if partial reduction of the Cu(II) may have occurred during X-ray diffraction data collection, two additional ligands with partial occupancy (~ 40%) are coordinated to the Cu(II) (Figure 2C). In the equatorial position, a water molecule is found at 2.6 Å from the copper ion in comparison to 1.8-2.3 Å in other Cu(II)-LPMO X-ray crystal structures.[80] This unusually long metal-ligand distance can be indicative of partial copper photoreduction leading to water discoordination.[82] This water molecule also donates a hydrogen bound to E60 (distance of 2.7 Å).

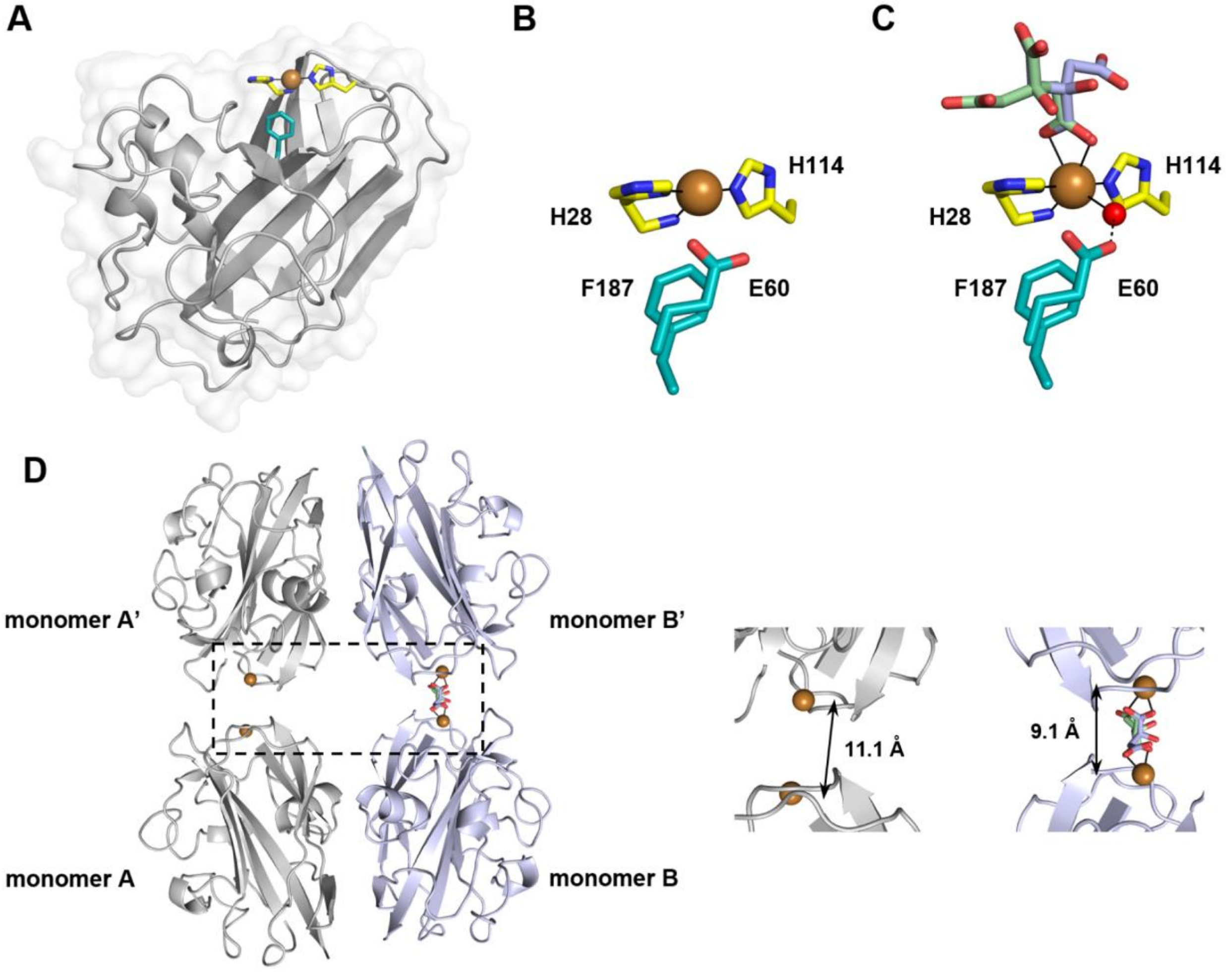

Figure 2. X-ray crystal structure of *Sm*AA10. (**A**) Global structure in grey cartoon featuring the two conserved active site histidine residues (C in yellow, N in dark blue) coordinating the copper ion (in brown), and the phenylalanine in axial (C in teal). (**B**) and (**C**) Zoom of the active site in monomers A and B corresponding to the Cu(I) and mixed Cu(I)/Cu(II) oxidation state, respectively. The first coordination sphere of the latter includes an equatorial water molecule (in red) H-bonding with E60 (C in teal, O in red), and a citrate buffer molecule (C in pale green for conformer A and in light blue for conformer B, O in red) in two alternative conformations with a carboxylate group as a bidentate ligand. (**D**) Structure of adjacent monomers in the crystal packing. Monomers A and B are facing symmetry-related monomers A' and B', respectively. Copper-

copper distance between monomers A is slightly higher than between monomers B, preventing their bridging through citrate coordination contrary to what is observed between monomers B.

In axial position, the Cu(II) is coordinated by the carboxylate group of a citrate buffer molecule in a bidentate fashion (Figure 2C). Interestingly, this citrate is found in two different conformations and bridges two monomers B from adjacent asymmetric units by copper coordination. This peculiar citrate coordination between two monomers does not seem to be possible for monomer A. Indeed, monomers A are slightly shifted in the crystal packing as indicated by the copper-copper distance between two adjacent monomers that increases from 9.1 to 11.1 Å for monomers B and A, respectively (Figure 2D). This prevents two neighboring carboxylate groups of a citrate molecule to coordinate the two copper ions at the same time. In addition to contributing to a strong crystal contact, the presence of the citrate buffer molecule yielded two distinct active site redox states: the fully reduced and the still significantly oxidized one (as citrate coordination prevented the active site Cu(II) ion to be fully photoreduced by X-rays during data collection).

Cu(II)-binding affinity

LPMOs are well-known to exhibit strong copper binding. Cu(II) affinity has been mostly studied by Isothermal Titration Calorimetry (ITC). Although ITC is often the method of choice to measure affinity constants, it can lead to significant underestimation of metal affinity since kinetic effects are not always taken into considerations binding competition with buffer molecules can exist and since correct metal speciation analysis is often lacking.[40] To avoid pitfalls associated with ITC, Cu(II) affinity for apo-*Sm*AA10 was re-evaluated using ligand competition and monitoring copper binding by intrinsic tryptophan fluorescence quenching (λ_{ex}= 290 nm and λ_{em}

= 340 nm). We first followed Cu(II) binding to *apo-Sm*AA10 and direct titration of apo-*Sm*AA10 by Cu(II) resulted in a linear quenching of tryptophan fluorescence up to a breakpoint at *ca*. one equivalent after which fluorescence remains constant (Figure S1), as observed for other bacterial LPMOs and other copper enzymes with strong binding affinity for copper.[21,83] This is consistent with a metal-to-protein binding stoichiometry of 1:1 and a strong binding affinity of *Sm*AA10 for Cu(II).

Chelators such as EDTA, EGTA or NTA with known Cu(II) affinity and forming stable 1:1 coordination complexes are commonly used in relation to the estimated affinity of the target metalloprotein.[40] The *apo*-protein (5 μM) was reconstituted with sub-stoichiometric amount of Cu(II) (from 1-5 μM) to ensure negligible contributions from low affinity ligands (*e.g.*, buffer) and from metal ion hydrolysis. The competitor ligand was then added in equimolar concentration (5 μM) and left to equilibrate before fluorescence was measured to estimate the fraction of metalated protein. Exchange of Cu(II) between the two ligands may be slow and to ensure that the system has reached equilibrium, we performed the same reaction starting from L-Cu(II) and adding *apo*-protein to the mixture. For *Sm*AA10, EGTA was chosen as the best competitor over EDTA or NTA as Cu(II) exchange with the protein was kinetically accessible after 24h (unlike with EDTA) and since competition with NTA appeared to be less favorable (Figure S2). The Cu(II) dissociation constant for *Sm*AA10 could be estimated at $K_D = 75 \pm 20$ fM at 25°C, which attests from the tight binding of Cu(II) to the histidine-brace ligands of *Sm*AA10. This value differs by several orders of magnitude with that previously measured by ITC (55 nM) for *Sm*AA10.[29] Our estimated Cu(II) dissociation constant is however consistent with that determined for the copper transporter CopC (10^{-13}-10^{-15} M) which harbors a similar Cu(II) coordination motif (histidine brace),[83] highlighting the fact that such coordinating motif offers a very strong binding to Cu(II).

Theoretical models of the Cu(II) and Cu(I) active sites

Theoretical calculations were performed in the Density Functional Theory (DFT) framework to support the experimental findings (see following sections) and get insight into the structures and properties of *Sm*AA10 LPMO active site.

Geometry optimization of *Sm*AA10-Cu(II) was undertaken on a structural model derived from the X-ray crystal structure and using monomer B as template (Figure 2C) while removing the citrate ligand and placing a water molecule. This model therefore includes two copper-bound water molecules and the two amino acids that directly coordinate the metal ion, namely His28 and His114. Second-sphere residues such as Gly29, Ser58, Ala112, Trp178, Ile180 and Phe187 were conserved. Distinct interactions between the protein envelope and the copper coordination sphere were accounted for with fragments of the amino acids Tyr30, Gln57, Leu59, Thr111, Arg113, Ser115, Thr116, Asp179, and Ala186. Long-range effects were included through implicit solvation while outer-layer crystallographically resolved solvent molecules were not conserved. The resulting DFT model presented in Figure 3A consists of 195 atoms and its key structural parameters shown in Table 2 are consistent with the crystallographic structure. The model has a five-coordinate Cu ion with two water ligands and two *N*-terminal histidine ligands. The N_3O_2 coordination sphere around the copper centre is compatible with a distorted geometry between trigonal bipyramidal and square pyramidal, consistent with crystallographic data.

A) *Sm*AA10-Cu(II)

B) *Sm*AA10-Cu(I)

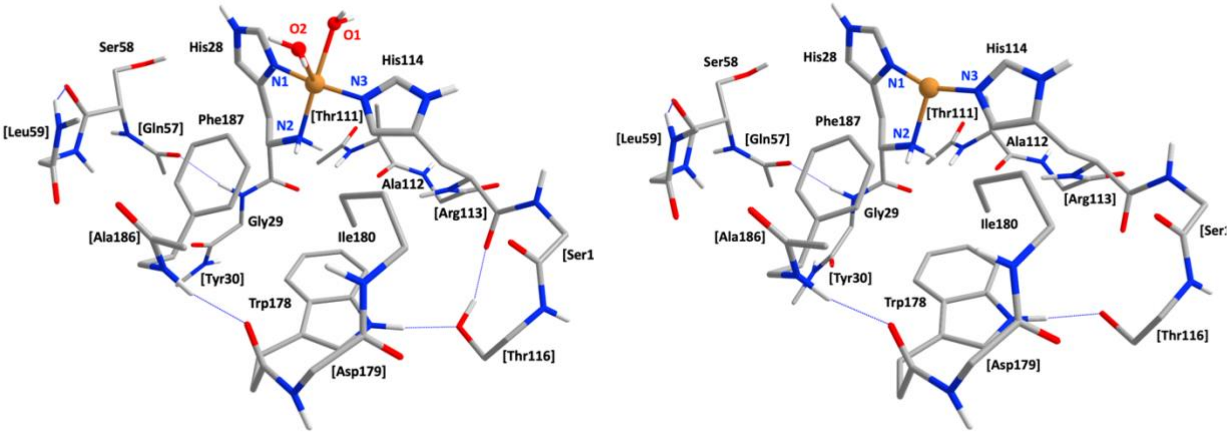

Figure 3. DFT models of *Sm*AA10-Cu(II) (**A**) and *Sm*AA10-Cu(I) (**B**) LPMO with the labels of the amino acids. Truncated peripheral residues denoted in square brackets and hydrogen atoms bonded to carbon centres are omitted for clarity.

Table 2. Selected structural parameters (distances in Å, angles in degrees) of the DFT models of the *Sm*AA10-Cu(II) and *Sm*AA10-Cu(I) LPMO active site. Experimental data are provided from monomer B (mixed Cu(II)/Cu(I) state) and monomer A (Cu(I)). Atom labelling is displayed in Figure S5.

	Parameters	Cu-N1 (H28 Im)	Cu-N2(NH$_2$)	Cu-N3 (H114)	Cu-O2	Cu-O1	N2-Cu-O2	N1-Cu-N2	N1-Cu-N3	N2-Cu-N3
Cu(II)	**Calc.**	1.975	2.144	2.007	2.431	2.234	121.6	90.8	171.3	93.7
	Exp.	1.97	2.16	1.96	2.60	2.30	116	96	172	92
Cu(I)	**Calc.**	1.918	2.219	1.915	-	-	-	96.8	156.8	106.2
	Exp.	1.95	2.16	1.89	-	-	-	97	169	94

The structural model used to describe the Cu(I) form of the active site consists of 189 atoms (Figure 3B) and its key structural parameters shown in Table 2. The Cu(I) model was obtained upon optimization of the Cu(II) model, after removing the two water molecules and changing the charge of the metal. The Cu(I) ion is bound to the two histidine ligands and features a three-coordinate T-shape geometry consistent with the solid-state structure of SmAA10 (monomer A), with the structural parameters comparing well to the ones obtained in the crystallographic structure. The Cu(I) ion is contained within a distorted plane with 3 nitrogen ligands, characterized by a calculated twist angle of 52.6 ° (X-Ray: 67.3 °). The distortion is also evidenced by the fact that the non-coordinating N-atoms are displaced from the DFT-predicted mean CuN3 plane from 0.242 to 0.601 Å (X-Ray: from 0.24 to 0.54 Å).

Spectroscopic properties of ***Sm*****AA10-Cu(II)**

EPR spectroscopy. EPR experiments were conducted for the oxidized enzyme placed in MES buffer at pH 6.5 (Figures 4 and S3). The echo-detected field-swept (EDSF) spectra were acquired by electron spin echo (ESE) detection at X- and Q-bands and processed using pseud-modulation. The resulting anisotropic signals are typical for Cu(II) species with the Q-band EDFS spectrum displaying well-resolved g-factor and hyperfine splitting pattern allowing their easy and accurate determination.

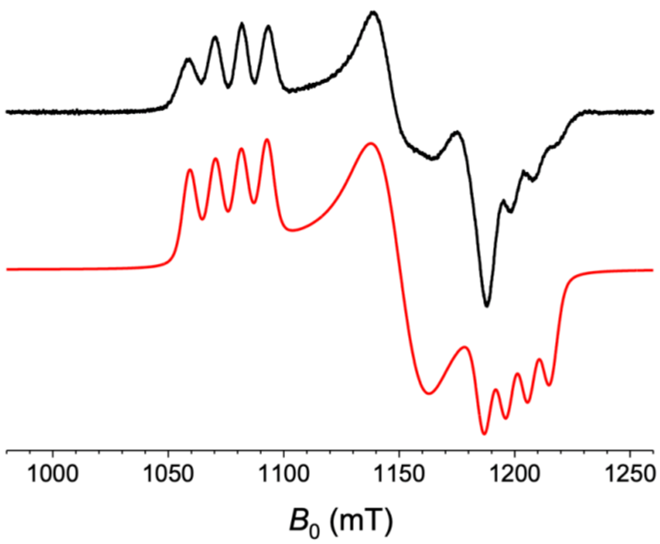

Figure 4. Pseudo-modulation of the EDFS (Q-band) recorded at 20 K of SmAA10-Cu(II) placed at 200 µM in 20 mM MES at pH = 6.5. Black line: experimental spectrum, red line: simulation.

Simulations of both Q-Band and X-band spectra using the EasySpin program package[41] provided *g*-factors and hyperfine coupling constants (hfcs) that are in good agreement with already reported ones (Table S2).[25] These data were further confronted with computations performed on the *Sm*AA10 DFT-model using the B3PW91 functional with 40% and 20% exact exchange admixture, respectively (Table 3). To assess the agreement between theory and experiment, we examined the axial and rhombic shift parameters (g_{max}, $A_{\text{max}}^{\text{Cu}}$, Δg and ΔA^{Cu}) as well as the isotropic values (g_{iso}, $A_{\text{iso}}^{\text{Cu}}$) and the results confirm that our DFT model reproduces quantitatively well the main features of the EPR spectrum of *Sm*AA10-Cu(II) at pH = 6.5.

Table 3. Comparison of the *g*-values and copper hyperfine coupling constants of *Sm*AA10-Cu(II) obtained from Easypsin simulations of Q-band spectrum and DFT computations.

	g-values			A^{Cu} (MHz)	
	Exp.	Calc.		Exp.	Calc.
g_1	2.258	2.271	A_1^{Cu}	375	396
g_2	2.114	2.120	A_2^{Cu}	57	84
g_3	2.024	2.048	A_3^{Cu}	268	268
g_{iso}	2.131	2.146	A_{iso}^{Cu}	233	249
Δg	0.234	0.223	ΔA^{Cu}	318	312

Both simulated and computed parameters provide three *g*-values that are consistent with a pentacoordinate rhombic geometry around the metal centre, intermediate between trigonal bipyramid and square pyramid.[84] This is consistent with the X-ray and DFT-optimized structures of *Sm*AA10-Cu(II). The sets of *g*-values also suggest that the singly occupied molecular orbital (SOMO) describing the ground state is a combination of the dz^2 and dx^2-y^2 orbitals. This is corroborated by electronic structure calculations which provide a Singly Occupied Molecular Orbital (SOMO, Figure S4) displaying a dominant Cu character (68%) and featuring an extended dz^2 orbital mixing (40%) into the dx^2-y^2 (60%), rationalizing thus the observed *g*-value rhombicity (Tables 3 and S2).

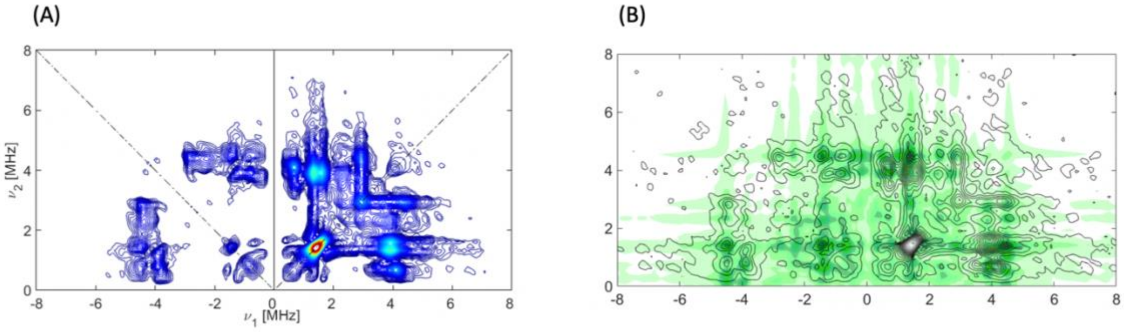

Figure 5. (A) **2D-**HYSCORE spectrum recorded at 20 K of *Sm*AA10-Cu(II) at pH 6.5 and (B) corresponding HYSCOREAN fit.

2D hyperfine sublevel correlation experiments (2D HYSCORE) were conducted at X-band to investigate in depth the coordination of the copper center. These experiments usually enable the proper assignment of various couplings arising from a broad range of nuclei such as ^{1}H, ^{13}C or ^{14}N. 2D HYSCORE experiments on *Sm*AA10-Cu(II) allow the detection of three distinct pairs of cross-peaks in the (+,+) quadrant (Figure 5A). Combining the experimental spectrum with the EasypSin-simulated one (Figure 5B) gives access to the values of the weak hfcs with nitrogen atoms (Table S3 and Figure S5 for atom labelling). These data are complemented by the simulated EDFS spectra that provide three sets of strong hfcs (with the Cu nuclei and 3 nitrogen atoms, Table S4). DFT-computations were then performed on the *Sm*AA10-Cu(II) model to predict the nitrogen hfcs in close proximity to the copper centre (Tables S5 and S6). Based on the good agreement between the simulated and calculated parameters, it is possible to ascribe the strong hfcs to the coordinating nitrogen centers of the His28 and His114 residues (N1, N2, N3 in Table S6, see Figure S5 for atom labelling). These results are consistent with previously reported data on a related chitin-active LPMO enzyme.[85] The weak hfcs originates both from the non-coordinated nitrogens of the imidazole groups of His28 and His114 and from the Gly29 residue (N4, N5, N6 in Table S5, see Figure S5 for atom labelling). These latter assignments are further supported by the good agreement between simulated and computed nuclear quadrupole coupling constants *K* (Tables S3 and S5). The comparison between experimental and computed isotropic values for the nitrogen hyperfine coupling constants is displayed in Table 4. Overall, by associating advanced EPR spectroscopic measurement to DFT calculations, we obtained a precise description of the coordination sphere and geometry of the metal centre in *Sm*AA10-Cu(II).

Table 4. Comparison of the isotropic values for nitrogen hyperfine coupling constants of *Sm*AA10-Cu(II) obtained from EasySpin simulations and DFT computations. Copper-bound nitrogens in bold.

Nuclei	**N1**$_{\mathrm{H28}}$	**N2**$_{\mathrm{NH2}}$	**N3**$_{\mathrm{H114}}$	N4$_{\mathrm{H28}}$	N5$_{\mathrm{H114}}$	N6$_{\mathrm{G29}}$
$A_{iso}^{expt.}$ (MHz)	36.29	39.12	32.75	2.14	1.90	1.36
$A_{iso}^{calc.}$ (MHz)	37.74	41.57	32.18	2.24	1.76	0.77

UV-Visible spectroscopy. The UV-visible spectrum (Figure 6A & S6A) of *Sm*AA10-Cu(II) displays a maximum at 675 nm (ε = 120 $M^{-1}.cm^{-1}$) with a shoulder around 800 nm (ε = 95 $M^{-1}.cm^{-1}$). Double d-d transitions are consistent with a distorted geometry around the copper center.[86] In addition, a transition is also observed around 340 nm (ε = 230 $M^{-1}.cm^{-1}$).

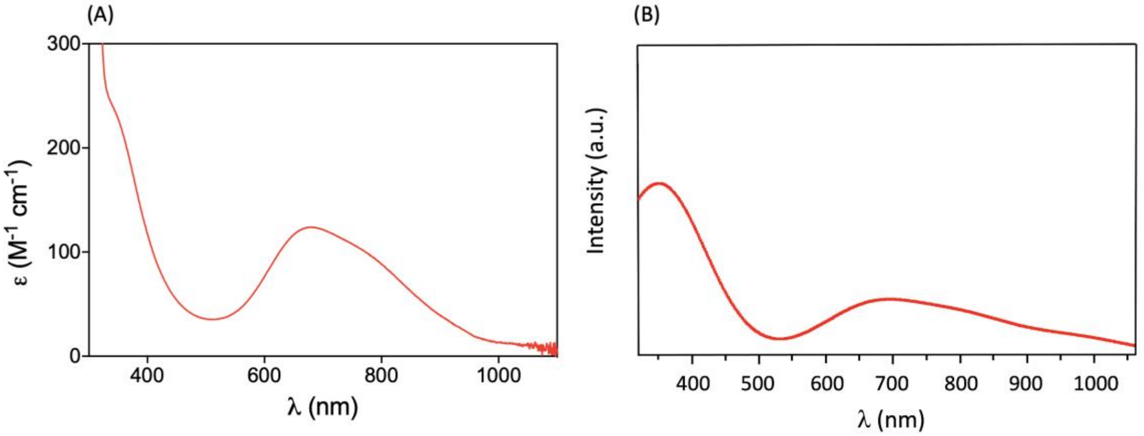

Figure 6. (A) UV-visible spectrum of *Sm*AA10-Cu(II) in 20 mM MES at pH 6.5 and (B) theoretical fit of the spectral features of the DFT model.

For a better understanding of the optical properties, TD-DFT calculations were undertaken on the *Sm*AA10-Cu(II) DFT-model to assign the features of the experimental UV-vis spectrum by computing the main transition energies and their relative intensities (Figures 6B and Figure S6B, Table S7). Our calculations adequately reproduce the key features of the spectrum in terms of energy and intensity, namely the band at 665 nm (calc: λ_{max} = 665 nm with f =0.086) and the shoulder at 800 nm (calc: λ_{max} = 800 nm with f =0.017) together with the slightly more intense absorption around 340 nm (calc: λ_{max} = 347 nm with f =0.013). The difference density plots presented in Figure S7 indicate that the two electronic transitions contributing to the shoulder observed at 800 nm are compatible with d-d- transitions while the band found at 665 nm arises from three main electronic transition displaying a mixed metal-ligand to metal character. For the more intense absorption found at 340 nm, two main transitions are identified and are assigned to ligand-to-metal charge transfer (LMCT) transitions. For all TDDFT-calculated electronic transitions, the acceptor orbital is the SOMO of Cu(II)-*Sm*AA10 (Figure S4) displaying 68% Cu

3d-character and 32% contribution ascribed to the nitrogen atoms from coordinating histidines which is further reflected in the nature of the computed UV-vis bands. Our calculations are overall in good agreement with the experimental data and corroborate well with our previous conclusions regarding the structural and electronic descriptions of Cu(II) ion in *Sm*AA10.

Spectroscopic features of *Sm*AA10-Cu(I)

The Partial Fluorescence Yield detected (PFY) Cu K-edge data collected on the ascorbic acid-reduced *Sm*AA10 (Figure 7A) exhibits a rising edge $1s \rightarrow 4p$ feature at 8983 eV with a shape and intensity consistent with a typical 3-coordinate Cu(I) center.[87] Furthermore, the k^3-weighted EXAFS exhibits a bimodal interference pattern at k ~4 $Å^{-1}$ typically seen in LPMO EXAFS and attributed to backscattering to outer shells of the histidine imidazole rings.[22,88–90] Initial fits (Table S8, Fits 1 and 2) of the Fourier Transformed EXAFS data (*k*-range 2 to 12 $Å^{-1}$) using FEFF calculated paths generated from the DFT geometry optimized structure suggest that the data could be fit with five unique paths (Fit 2). Further optimization of path distances (Fits 3-7) suggests Cu–N_{His} distances slightly contracted from the geometry-optimized structure (0.03 Å shorter). Overall, however, the path distances do not significantly deviate from the distances suggested by the geometry-optimized structure. Attempts to model an additional O ligand as water upon a 4-coordinate Cu site did not improve the fit. It was found that fits of the Cu-$C_{2/3}$ path (R = ~3.22 Å) recurrently converged upon a model with negative a Debye-Waller factor (σ^2), which describes the variance in R due to static and thermal disorder (and therefore cannot be negative). Restraining the model to $\sigma^2 = 2\times10^{-3}$ $Å^2$ for the path did provide a reasonable fit (Table S8, Fit 8), with differences being well within the noise level of the data (Figure S8). Alternatively, increasing the degeneracy of the Cu-$C_{2/3}$ path to $N = 3$ (Fit 9) provided a slightly better fit. However, a chemical rationalization for the increased degeneracy could not be justified, even when accounting for atoms from secondary sphere residues (*e.g.* F187). Attempts to restrain or correlate $\sigma^2_{\text{Cu-C2/3}}$ with $\sigma^2_{\text{Cu-N5/9}}$ provided unsatisfactory results. The introduction of a Cu···$\text{N}_{5/9}$···$\text{C}_{4/6/10/13}$ multiple scattering path, and omission of the weak Cu-$\text{C}_{2/3}$ path (Table S8, Fit 13) provided the more chemically sensible fit. However, restraining the σ^2 of the Cu-$\text{C}_{4/6/10/13}$ path was found to be necessary (Table S8, Fit 14). Further attempts to improve the fit were unsatisfactory. Thus, we conclude that Fit 14 provides the most reasonable fit grounded within the limits of the expected structure for *Sm*AA10-Cu(I).

The PFY-detected data resolution is a convolution of the Cu core-hole lifetime energy broadening (2.11 eV for Cu $\text{K}\alpha_1$)[91] and the broadening contribution based on the Darwin width of the monochromator (1.15 eV for Si(111) at 9 keV). The resulting energy broadening is then determined to be a theoretical 2.40 eV. In contrast, in High-Energy Resolution Fluorescence Detected XAS, the core hole broadening is sharpened to 0.53 eV (Γ_{APP} derived from K and L_3 core holes of the intermediate and final states, respectively). The observed energy resolution of the experimental configuration was determined to be 0.6 eV based on the elastic line at 8046 eV, giving an improved overall spectral broadening of 0.96 eV. Consequently, the 1*s*→4*p* rising edge feature at 8983 eV in the PFY data was resolved into a sharp peak at 8982.2 eV and a higher-energy shoulder at 8983.8 eV. The calculated XAS spectrum using DFT model of *Sm*AA10-Cu(I) LPMO (Figure 7B) adequately reproduces the rising edge feature associated with the transition to Cu(4p_z) aligned perpendicular to the plane formed with the two coordinating nitrogen centers of the His28 residue. The intensity modulation at energies above the main feature is also captured, and clearly seen when the calculated spectrum is convoluted with a linewidth more comparable with the experimental energy resolution.

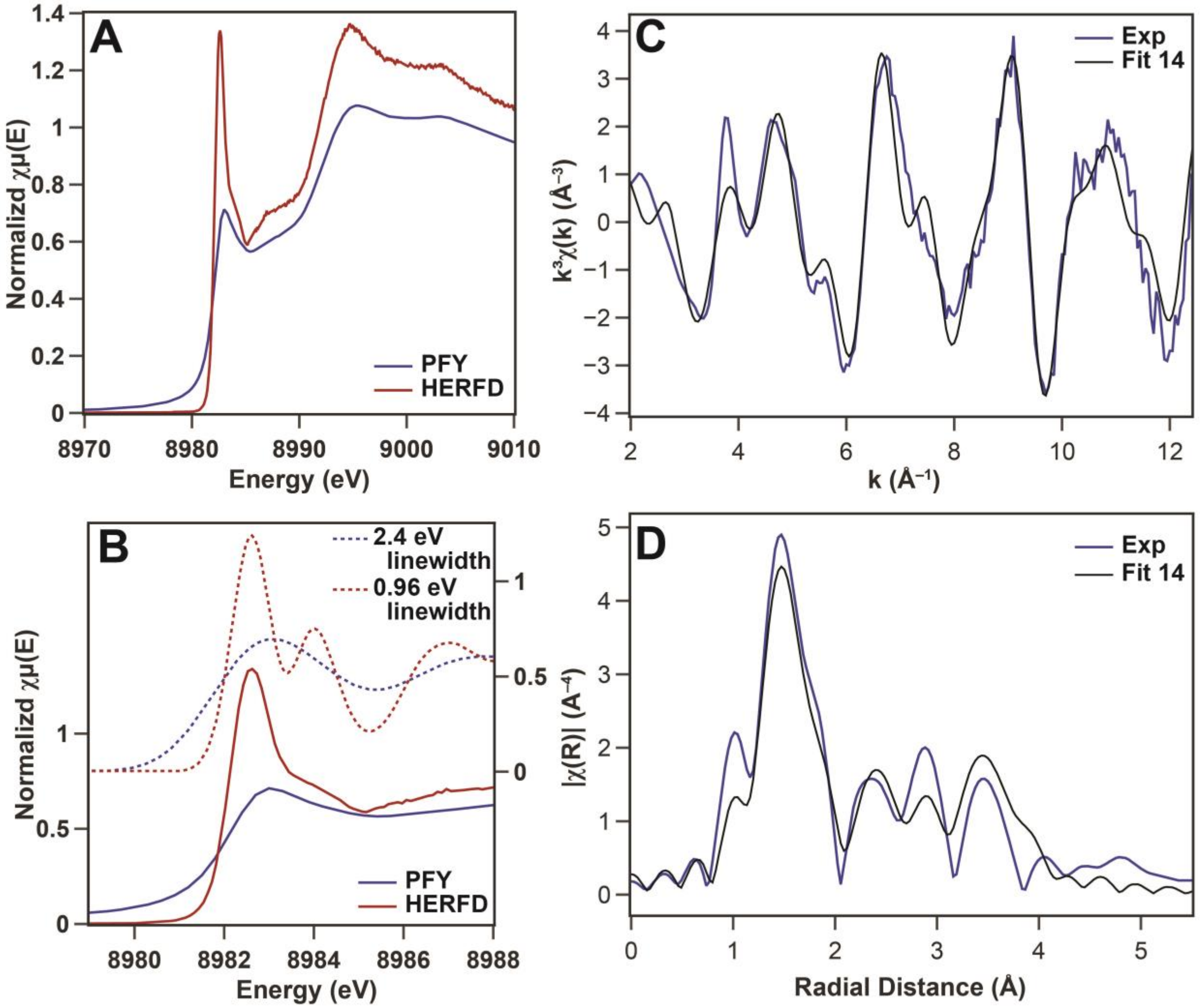

Figure 7. (A) Cu K-edge X-ray absorption data for *Sm*AA10-Cu(I) detected in PFY (blue) and HERFD (red) configurations. The Cu K-edge data have been normalized by the edge jump (see Supporting Information). (B, *top*) TDDFT calculated XANES spectra for DFT model of Cu(I)-*Sm*AA10 LPMO applying an energy shift of –4.24 eV using Gaussian line shape widths of 2.40 eV (blue) and 0.96 eV (red) together with experimental data (*bottom*). Note that the y-axis is on the right for the calculated spectra and on the left for the experimental data. (C) k^3-weighted

EXAFS and Fit 14 (Table S8). (D) Non-phase shifted Fourier transform over a *k*-range of 2 to 12 $Å^{-1}$ and Fit 14 (Table S8).

Additionally, the contributions from each 4p orbital could be inferred from the calculated polarizations, shown in Figure 8A. The rising edge main feature at 8982.2 eV is dominated by the $4p_z$ orbital (perpendicular to Cu-N bonds in His28, as shown in Figure 8B), with contributions from the $4p_x$ orbital (lying along Cu-terminal amine of His28) especially on the low-energy side of the main feature. For the broad features at 8984 and 8987 eV, the $4p_x$ is the major source of intensity, followed by $4p_z$. Finally, the $4p_y$ orbital (along the Cu-imidazole axis) contributes the least throughout, but more importantly towards higher energy. This analysis highlights the sensitivity of HERFD XAS to active site geometry, and its promise for broader applications to copper-based enzymes and catalysts.

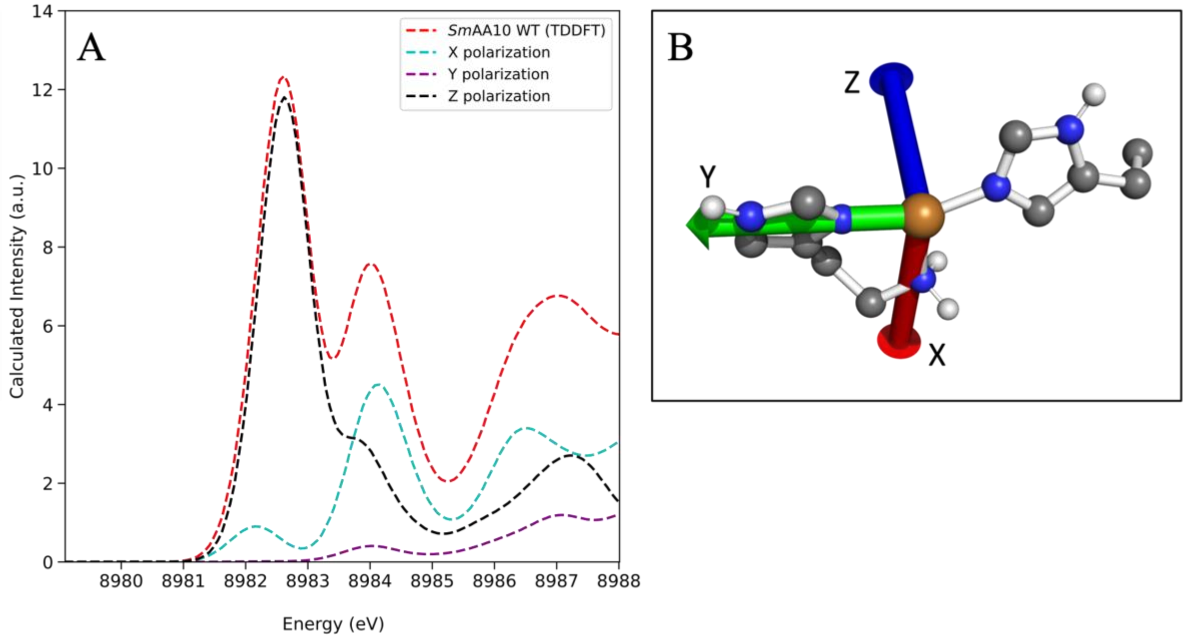

Figure 8. A) TD-DFT calculated spectra of *Sm*AA10-Cu(I) K-edge with XYZ polarization components with HERFD broadening (0.96 eV). B) Orientation of the histidine brace in the cluster model is such that the y axis lies along Cu-N bond involving the His28 imidazole ring and x axis is along Cu-NH_2 involving the His28 primary amine.

Redox properties

*Sm*AA10 Cu(II)/Cu(I) redox potential was previously determined using *N,N,N',N'*-tetramethyl-1,4-phenylenediamine (TMP) as a chromogenic redox indicator at 275 mV *vs.* NHE (at pH 6).[29] Following a similar protocol with the same redox mediator, we found a similar value of 280 ± 15 mV *vs.* NHE (pH 6.5).

As the previous method is indirect, we investigated the redox properties of *Sm*AA10 using cyclic voltammetry. *Sm*AA10-Cu(II) was casted on the surface of a modified PG electrode and entrapped using a dialysis membrane. The cyclic voltammograms of *Sm*AA10 demonstrated oxidation and reduction currents increase, yet without characteristic peaks at scan rates > 2 mV/s

(Figure S10). Well-shaped symmetric peaks typical for the thin layer configuration were only obtained at very low scan rates such as 0.05 mV/s (Figure 9A). This indicates that the rate of the Cu(II)/Cu(I) *Sm*AA10 redox transition is very slow compared to that observed for other small copper containing proteins.[92,93] Using cyclic voltammetry, we determined a redox potential of 360 ± 10 mV *vs.* NHE for Cu(II)/Cu(I) in *Sm*AA10 (as measured for two independent enzyme preparations)

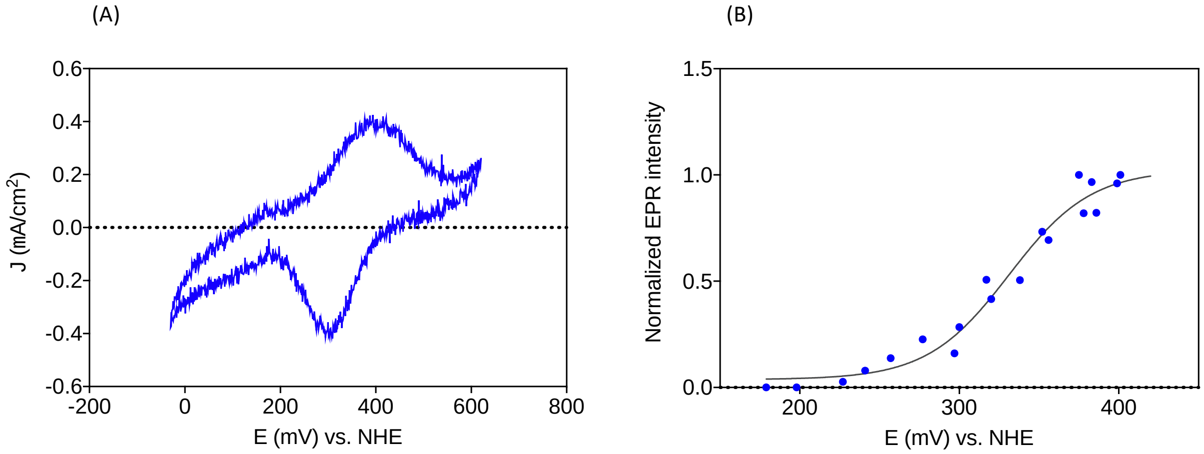

Figure 9. A) CV of *Sm*AA10 at 0.05 mV/s B) Redox titration of *Sm*AA10 at 298 K followed by EPR. The curve was simulated using Nernst equation and one electron exchanged.

As the redox potential obtained using a redox indicator or by cyclic voltammetry are not consistent (80 mV difference), we further investigated the redox properties of *Sm*AA10 by redox titration monitored by EPR. Using this approach, we determined a redox potential value of 350 ± 10 mV *vs.* NHE for Cu(II)/Cu(I) *Sm*AA10, which is consistent with that obtained by cyclic voltammetry (Figure 9B).

These results significantly differ from previously reported values obtained by indirect method using TMP as a redox indicator. There are few direct electrochemical measurements of redox potentials for LPMO enzymes.[94–96] The use of indirect method can lead to errors or imprecisions as the choice of the redox indicator as well as the strict control of anaerobicity can induce non-negligible bias on the measurements. Indeed, Hemsworth *et al.*, have previously reported that the choice of the redox indicator could lead to discrepancies in the determination of accurate redox potentials.[81] For instance, they measured a redox potential for the chitin-active LPMO from *Bacillus amyloliquefaciens* (*Ba*AA10) that ranges from 275 to 370 mV *vs.* NHE using either thionine, TMP, or 2,6-dichlorophenolindophenol as redox indicator. In the present case, we validated cyclic voltammetry and redox titration monitored by EPR as preferred techniques for consistent redox potential measurement.

The experimentally-determined redox potential was confronted with DFT calculations using the DFT models presented in Figure 3 for both *Sm*AA10-Cu(II) and Cu(I), respectively. Our calculations provided a computed redox potential of +348 mV *vs.* NHE (Tables S9 and S10), a value in good agreement with the above measurements thus supporting both the coordination geometries of the oxidized and reduced copper ion in *Sm*AA10 and the suggested approach to experimentally determine this thermodynamic parameter.

Estimation of the dissociation constant for Cu(I).

Following an already reported approach,[29] we have estimated the dissociation constant of Cu(I) to *Sm*AA10 thanks to a thermodynamical cycle and using the redox potentials of *Sm*AA10-Cu(II)/ *Sm*AA10-Cu(I) and free Cu(II)/Cu(I) as well as the *Sm*AA10-Cu(II) dissociation constant. Details about this calculation are included in Supplementary Information. The value points towards a very high affinity for Cu(I) with a calculated K_D^I for *Sm*AA10-Cu(I) of 5.6×10^{-17}. This value is significantly lower than that already reported for *Sm*AA10,[29] reflecting the differences in the experimentally determined values of redox potential and copper(II) dissociation constant.

Conclusion

*Sm*AA10 in a model bacterial LPMO that has been widely investigated in the past. In the present paper, we have carried out a comprehensive investigation of the copper active site properties combining experimental and theoretical approaches.

Firstly, we have successfully obtained crystallographic data of the metalated enzyme, representing key structural and yet missing data for the investigation of the architecture and coordination environment of the copper center. We have then measured the copper binding affinity using a robust methodology based on the use of competing ligands and avoiding the pitfalls of excess free metal ions and competition with buffer molecules. Following this methodology, we determine a significantly tighter copper binding to the histidine brace ligands than previously reported. Then, spectroscopic techniques including UV-Visible spectroscopy, advanced EPR techniques and PFY and HERFD XAS, have allowed us to probe the electronic structure and coordination geometry of the copper active site at both the Cu(II) and Cu(I) redox states. These experimental data were rationalized by DFT calculations enriching our comprehension of the electronic structure of the copper sites within the histidine brace ligands. Finally, the Cu(II)-Cu(I) redox potential was determined using two independent techniques and supported by theoretical calculations based on the previously validated DFT models. Notably, the redox potential is determined at a higher value than previously reported, shedding light on the electron transfer capabilities of the copper center within *Sm*AA10.

Data on the electronic structure of LPMO active site are of high importance for the debate on monooxygenase *vs*. peroxygenase mechanisms. It is proposed that reduction to the copper(I) state precedes binding of the extended substrate and reaction with either O_2 or H_2O_2.[15] Notably, binding of the substrate significantly affects the active site properties at the Cu(II) redox state.[25,85,97,98] It would therefore be essential to obtain accurate electronic descriptions in the presence of substrate. It is important to note that *Sm*AA10-Cu(II)/ *Sm*AA10-Cu(I) redox potential is rather high (*ca*. 350 mV *vs*. NHE). A recent investigation has reported that binding of the polysaccharidic substrate increases the redox potential of a fungal AA9 LPMO.[13] Interestingly, the $E_{1/2}$ of Cu(II)/Cu(I) redox couple of small copper-containing complexes was shown to correlate with the binding energy of O_2 to Cu(I) with more electron-rich copper centers (lower redox potentials) binding O_2 more strongly.[99] In the same study, a relation has been established between the $E_{1/2}$ and the ability to electrochemically reduce O_2 *vs* H_2O_2 and it was observed that increasing $E_{1/2}$ lowers the electrocatalytic rate for both O_2 and H_2O_2 reduction but in a different extent, leading to a change in the relative magnitude between both reactions. At higher $E_{1/2}$, reduction of H_2O_2 was favored over the reduction of O_2. These findings suggest that binding of the substrate to LPMO could favor reaction with H_2O_2 as compared to O_2. This conclusion is in line with findings that oxidation of LPMO–Cu(I) is several orders of magnitude faster with H_2O_2 than with O_2.[100,101] However, more data on substrate-bound LPMO-Cu(I) are necessary to get insight into this important debate. Our proposed methodology combining experimental and theoretical approaches provides a solid background for such investigations.

In summary, this study advances our knowledge of the copper active site properties of a model bacterial enzyme, *Sm*AA10, emphasizing the importance of combining experimental and theoretical approaches. This integrated strategy moreover appears as a powerful methodology to the broader understanding of copper-containing metalloenzymes, a key step towards their application in biotechnological processes or the rational design of efficient bioinspired catalysts.

ASSOCIATED CONTENT

Supporting Information.

Supporting Information: Additional experimental details (gene cloning, protein expression and purification) and additional experimental data including Cartesian coordinates of the DFT models (PDF).

AUTHOR INFORMATION

Corresponding Authors

* Corresponding authors: serena.debeer@cec.mpg.de, maylis.orio@univ-amu.fr, decroosc@igbmc.fr and jalila.simaan@univ-amu.fr.

Present Address

§ INRAE, Aix Marseille Univ., UMR1163 Biodiversité et Biotechnologie Fongiques, 13009
Marseille, France

Author Contributions

The manuscript was written through contributions of all authors. All authors have given approval to the final version of the manuscript.

‡These authors contributed equally

Funding Sources

This project was supported by the CNRS, Aix Marseille Université, the Agence Nationale de la Recherche (Abiozyme, ANR-18-CE07-0003) including a doctoral fellowship to MP, and the

French Ministère de l'Enseignement Supérieur et de la Recherche for a doctoral fellowship to AM. Financial support from the IR INFRANALYTICS FR2054 for conducting the research is gratefully acknowledged. The authors thank Claude Arnold for assistance and management of computer ressources. A.T., C. J., S.A.V.J. and S.D. acknowledge funding from the European Research Council (ERC) through a Synergy Grant (856446), Max-Planck-Gesellschaft, and Alexander von Humboldt Research Fellowship (C.J.).

Notes

Data for the XAS analysis can be found using the following reference: Joseph, C.; DeBeer, S. Cu K-alpha HERFD-XANES of SmAA10-Cu(I). European Synchrotron Radiation Facility 2024. https://doi.org/10.15151/ESRF-DC-1469091709

ACKNOWLEDGMENT

The authors gratefully acknowledge Ole Golten and Vincent G. H. Eijsink (*Norwegian University of Life Sciences*, *NMBU*) for provision of supplemental *Sm*AA10 protein used for X-ray spectroscopic data collection. *Diamond Light Source* is gratefully acknowledged for provision of time at the I20-scanning beamline (SP31504) for the PFY-XAS data, as well as Dr. Matteo Aramini, Dr. Liqun Kang, Dr. Kushal Sengupta, and Dr. Maria Alessandra Martini for assistance at the beamtime. The authors additionally acknowledge the *European Synchrotron Radiation Facility* (*ESRF*) for time at the ID26 beamline (CH6670) for the HERFD-XAS data, as well as Dr. Sami Vasala, Dr. Pieter Glatzel, and Dr. George E. Cutsail III for assistance at the beamtime. We also acknowledge the French Biology/Health beamtime allocation committee for provision of beamtime on beamline BM07-FIP2 at the European Synchrotron Radiation Facility under proposal number a07-1-8, and we would like to thank the local contacts Sylvain Engilberge and Eric Mathieu for assistance in using the beamline.

ABBREVIATIONS

AA, auxiliary activity; CAZyme, carbohydrate-active enzyme; LPMO, lytic polysaccharide monooxygenase; rmsd, root-mean-square deviation; DFT, density functional theory; EPR, electron paramagnetic resonance, EDSF, echo-detected field-swept; HYSCORE, hyperfine sublevel correlation; TMP, *N,N,N',N'*-tetramethyl-1,4-phenylenediamine; EDTA, *N*,*N*,*N*′,*N*′-ethylenediamine tetraacetic acid; EGTA, ethyleneglycol-*O*,*O*′-bis(2-aminoethyl)-*N*,*N*,*N*′,*N*′-tetraacetic acid; NTA, nitrilotriacetic acid; HERFD high energy resolution fluorescence detection; PFY, partial fluorescence yield; XAS, X-ray absorption spectroscopy

REFERENCES

(1) Tuck, C. O.; Pérez, E.; Horváth, I. T.; Sheldon, R. A.; Poliakoff, M. Valorization of Biomass: Deriving More Value from Waste. *Science* **2012**, *337* (6095), 695–699. https://doi.org/10.1126/science.1218930.

(2) Vaaje-Kolstad, G.; Westereng, B.; Horn, S. J.; Liu, Z.; Zhai, H.; Sørlie, M.; Eijsink, V. G. H. An Oxidative Enzyme Boosting the Enzymatic Conversion of Recalcitrant Polysaccharides. *Science* **2010**, *330* (6001), 219–222. https://doi.org/10.1126/science.1192231.

(3) Quinlan, R. J.; Sweeney, M. D.; Leggio, L. L.; Otten, H.; Poulsen, J.-C. N.; Johansen, K. S.; Krogh, K. B. R. M.; Jørgensen, C. I.; Tovborg, M.; Anthonsen, A.; Tryfona, T.; Walter, C. P.; Dupree, P.; Xu, F.; Davies, G. J.; Walton, P. H. Insights into the Oxidative Degradation of Cellulose by a Copper Metalloenzyme That Exploits Biomass Components. *Proc. Natl. Acad. Sci.* **2011**, *108* (37), 15079–15084. https://doi.org/10.1073/pnas.1105776108.

(4) Hemsworth, G. R.; Johnston, E. M.; Davies, G. J.; Walton, P. H. Lytic Polysaccharide Monooxygenases in Biomass Conversion. *Trends Biotechnol.* **2015**, *33* (12), 747–761. https://doi.org/10.1016/j.tibtech.2015.09.006.

(5) Tandrup, T.; Frandsen, K. E. H.; Johansen, K. S.; Berrin, J.-G.; Leggio, L. L. Recent Insights into Lytic Polysaccharide Monooxygenases (LPMOs). *Biochem. Soc. Trans.* **2018**, *46* (6), 1431–1447. https://doi.org/10.1042/bst20170549.

(6) Hangasky, J. A.; Detomasi, T. C.; Marletta, M. A. Glycosidic Bond Hydroxylation by Polysaccharide Monooxygenases. *Trends Chem.* **2019**, *1* (2), 198–209. https://doi.org/10.1016/j.trechm.2019.01.007.

(7) Forsberg, Z.; Sørlie, M.; Petrović, D.; Courtade, G.; Aachmann, F. L.; Vaaje-Kolstad, G.; Bissaro, B.; Røhr, Å. K.; Eijsink, V. G. Polysaccharide Degradation by Lytic Polysaccharide Monooxygenases. *Curr. Opin. Struct. Biol.* **2019**, *59*, 54–64. https://doi.org/10.1016/j.sbi.2019.02.015.

(8) Bissaro, B.; Røhr, Å. K.; Müller, G.; Chylenski, P.; Skaugen, M.; Forsberg, Z.; Horn, S. J.; Vaaje-Kolstad, G.; Eijsink, V. G. H. Oxidative Cleavage of Polysaccharides by Monocopper Enzymes Depends on H2O2. *Nat. Chem. Biol.* **2017**, *13* (10), 1123–1128. https://doi.org/10.1038/nchembio.2470.

(9) Schwaiger, L.; Csarman, F.; Chang, H.; Golten, O.; Eijsink, V. G. H.; Ludwig, R. Electrochemical Monitoring of Heterogeneous Peroxygenase Reactions Unravels LPMO Kinetics. *ACS Catal.* **2024**, *14* (2), 1205–1219. https://doi.org/10.1021/acscatal.3c05194.

(10) Meier, K. K.; Jones, S. M.; Kaper, T.; Hansson, H.; Koetsier, M. J.; Karkehabadi, S.; Solomon, E. I.; Sandgren, M.; Kelemen, B. Oxygen Activation by Cu LPMOs in Recalcitrant Carbohydrate Polysaccharide Conversion to Monomer Sugars. *Chem. Rev.* **2018**, *118* (5), 2593–2635. https://doi.org/10.1021/acs.chemrev.7b00421.

(11) Wang, B.; Wang, Z.; Davies, G. J.; Walton, P. H.; Rovira, C. Activation of O2 and H2O2 by Lytic Polysaccharide Monooxygenases. *ACS Catal.* **2020**, *10* (21), 12760–12769. https://doi.org/10.1021/acscatal.0c02914.

(12) Rieder, L.; Petrović, D.; Väljamäe, P.; Eijsink, V. G. H.; Sørlie, M. Kinetic Characterization of a Putatively Chitin-Active LPMO Reveals a Preference for Soluble Substrates and Absence of Monooxygenase Activity. *Acs Catal* **2021**, *11* (18), 11685–11695. https://doi.org/10.1021/acscatal.1c03344.

(13) Hedison, T. M.; Breslmayr, E.; Shanmugam, M.; Karnpakdee, K.; Heyes, D. J.; Green, A. P.; Ludwig, R.; Scrutton, N. S.; Kracher, D. Insights into the H2O2-driven Catalytic Mechanism of Fungal Lytic Polysaccharide Monooxygenases. *FEBS J.* **2021**, *288* (13), 4115–4128. https://doi.org/10.1111/febs.15704.

(14) Hangasky, J. A.; Iavarone, A. T.; Marletta, M. A. Reactivity of O2 versus H2O2 with Polysaccharide Monooxygenases. *Proc. Natl. Acad. Sci.* **2018**, *115* (19), 4915–4920. https://doi.org/10.1073/pnas.1801153115.

(15) Munzone, A.; Eijsink, V. G. H.; Berrin, J.-G.; Bissaro, B. Expanding the Catalytic Landscape of Metalloenzymes with Lytic Polysaccharide Monooxygenases. *Nat. Rev. Chem.* **2024**, *8* (2), 106–119. https://doi.org/10.1038/s41570-023-00565-z.

(16) Vandhana, T. M.; Reyre, J.; Sushmaa, D.; Berrin, J.; Bissaro, B.; Madhuprakash, J. On the Expansion of Biological Functions of Lytic Polysaccharide Monooxygenases. *New Phytol* **2022**, *233* (6), 2380–2396. https://doi.org/10.1111/nph.17921.

(17) Drula, E.; Garron, M.-L.; Dogan, S.; Lombard, V.; Henrissat, B.; Terrapon, N. The Carbohydrate-Active Enzyme Database: Functions and Literature. *Nucleic Acids Res.* **2021**, *50* (D1), D571–D577. https://doi.org/10.1093/nar/gkab1045.

(18) Lawton, T. J.; Kenney, G. E.; Hurley, J. D.; Rosenzweig, A. C. The CopC Family: Structural and Bioinformatic Insights into a Diverse Group of Periplasmic Copper Binding Proteins. *Biochemistry* **2016**, *55* (15), 2278–2290. https://doi.org/10.1021/acs.biochem.6b00175.

(19) Jodts, R. J.; Ross, M. O.; Koo, C. W.; Doan, P. E.; Rosenzweig, A. C.; Hoffman, B. M. Coordination of the Copper Centers in Particulate Methane Monooxygenase: Comparison between Methanotrophs and Characterization of the CuC Site by EPR and ENDOR Spectroscopies. *J Am Chem Soc* **2021**, *143* (37), 15358–15368. https://doi.org/10.1021/jacs.1c07018.

(20) Fisher, O. S.; Sendzik, M. R.; Ross, M. O.; Lawton, T. J.; Hoffman, B. M.; Rosenzweig, A. C. PCuAC Domains from Methane-Oxidizing Bacteria Use a Histidine Brace to Bind Copper. *J. Biol. Chem.* **2019**, *294* (44), 16351–16363. https://doi.org/10.1074/jbc.ra119.010093.

(21) Munzone, A.; Kerdi, B. E.; Fanuel, M.; Rogniaux, H.; Ropartz, D.; Réglier, M.; Royant, A.; Simaan, A. J.; Decroos, C. Characterization of a Bacterial Copper-dependent Lytic Polysaccharide Monooxygenase with an Unusual Second Coordination Sphere. *FEBS J.* **2020**, *287* (15), 3298–3314. https://doi.org/10.1111/febs.15203.

(22) Hall, K. R.; Joseph, C.; Ayuso-Fernández, I.; Tamhankar, A.; Rieder, L.; Skaali, R.; Golten, O.; Neese, F.; Røhr, Å. K.; Jannuzzi, S. A. V.; DeBeer, S.; Eijsink, V. G. H.; Sørlie, M. A Conserved Second Sphere Residue Tunes Copper Site Reactivity in Lytic Polysaccharide Monooxygenases. *J. Am. Chem. Soc.* **2023**, *145* (34), 18888–18903. https://doi.org/10.1021/jacs.3c05342.

(23) Li, X.; Beeson, W. T.; Phillips, C. M.; Marletta, M. A.; Cate, J. H. D. Structural Basis for Substrate Targeting and Catalysis by Fungal Polysaccharide Monooxygenases. *Structure* **2012**, *20* (6), 1051–1061. https://doi.org/10.1016/j.str.2012.04.002.

(24) Gudmundsson, M.; Kim, S.; Wu, M.; Ishida, T.; Momeni, M. H.; Vaaje-Kolstad, G.; Lundberg, D.; Royant, A.; Stahlberg, J.; Eijsink, V. G. H.; Beckham, G. T.; Sandgren, M. Structural and Electronic Snapshots during the Transition from a Cu(II) to Cu(I) Metal Center of a Lytic Polysaccharide Monooxygenase by X-Ray Photoreduction. *J. Biol. Chem.* **2014**, *289* (27), 18782–18792. https://doi.org/10.1074/jbc.m114.563494.

(25) Bissaro, B.; Isaksen, I.; Vaaje-Kolstad, G.; Eijsink, V. G. H.; Røhr, Å. K. How a Lytic Polysaccharide Monooxygenase Binds Crystalline Chitin. *Biochemistry* **2018**, *57* (12), 1893–1906. https://doi.org/10.1021/acs.biochem.8b00138.

(26) Forsberg, Z.; Røhr, Å. K.; Mekasha, S.; Andersson, K. K.; Eijsink, V. G. H.; Vaaje-Kolstad, G.; Sørlie, M. Comparative Study of Two Chitin-Active and Two Cellulose-Active AA10-Type Lytic Polysaccharide Monooxygenases. *Biochemistry* **2014**, *53* (10), 1647–1656. https://doi.org/10.1021/bi5000433.

(27) Vaaje-Kolstad, G.; Horn, S. J.; Sørlie, M.; Eijsink, V. G. H. The Chitinolytic Machinery of S Erratia Marcescens – a Model System for Enzymatic Degradation of Recalcitrant Polysaccharides. *FEBS J.* **2013**, *280* (13), 3028–3049. https://doi.org/10.1111/febs.12181.

(28) Vaaje-Kolstad, G.; Houston, D. R.; Riemen, A. H. K.; Eijsink, V. G. H.; Aalten, D. M. F. van. Crystal Structure and Binding Properties of the Serratia Marcescens Chitin-Binding Protein CBP21*. *J. Biol. Chem.* **2005**, *280* (12), 11313–11319. https://doi.org/10.1074/jbc.m407175200.

(29) Aachmann, F. L.; Sørlie, M.; Skjåk-Bræk, G.; Eijsink, V. G. H.; Vaaje-Kolstad, G. NMR Structure of a Lytic Polysaccharide Monooxygenase Provides Insight into Copper Binding, Protein Dynamics, and Substrate Interactions. *Proc. Natl. Acad. Sci.* **2012**, *109* (46), 18779–18784. https://doi.org/10.1073/pnas.1208822109.

(30) Kont, R.; Bissaro, B.; Eijsink, V. G. H.; Väljamäe, P. Kinetic Insights into the Peroxygenase Activity of Cellulose-Active Lytic Polysaccharide Monooxygenases (LPMOs). *Nat. Commun.* **2020**, *11* (1), 5786. https://doi.org/10.1038/s41467-020-19561-8.

(31) Munzone, A. Structure-Reactivity Relationship of the Copper-Dependent Lytic Polysaccharide MonoOxygenase., Aix Marseille Université, 2021.

(32) Kowalska, J. K.; Lima, F. A.; Pollock, C. J.; Rees, J. A.; DeBeer, S. A Practical Guide to High-resolution X-ray Spectroscopic Measurements and Their Applications in Bioinorganic Chemistry. *Isr. J. Chem.* **2016**, *56* (9–10), 803–815. https://doi.org/10.1002/ijch.201600037.

(33) III, G. E. C.; DeBeer, S. Challenges and Opportunities for Applications of Advanced X-Ray Spectroscopy in Catalysis Research. *ACS Catal.* **2022**, *12* (10), 5864–5886. https://doi.org/10.1021/acscatal.2c01016.

(34) Vonrhein, C.; Flensburg, C.; Keller, P.; Sharff, A.; Smart, O.; Paciorek, W.; Womack, T.; Bricogne, G. Data Processing and Analysis with the AutoPROC Toolbox. *Acta Crystallogr. Sect. D* **2011**, *67* (4), 293–302. https://doi.org/10.1107/s0907444911007773.

(35) Monaco, S.; Gordon, E.; Bowler, M. W.; Delagenière, S.; Guijarro, M.; Spruce, D.; Svensson, O.; McSweeney, S. M.; McCarthy, A. A.; Leonard, G.; Nanao, M. H. Automatic Processing of Macromolecular Crystallography X-Ray Diffraction Data at the ESRF. *J. Appl. Crystallogr.* **2013**, *46* (3), 804–810. https://doi.org/10.1107/s0021889813006195.

(36) Delagenière, S.; Brenchereau, P.; Launer, L.; Ashton, A. W.; Leal, R.; Veyrier, S.; Gabadinho, J.; Gordon, E. J.; Jones, S. D.; Levik, K. E.; McSweeney, S. M.; Monaco, S.; Nanao, M.; Spruce, D.; Svensson, O.; Walsh, M. A.; Leonard, G. A. ISPyB: An Information Management System for Synchrotron Macromolecular Crystallography. *Bioinformatics* **2011**, *27* (22), 3186–3192. https://doi.org/10.1093/bioinformatics/btr535.

(37) McCoy, A. J.; Grosse-Kunstleve, R. W.; Adams, P. D.; Winn, M. D.; Storoni, L. C.; Read, R. J. Phaser Crystallographic Software. *J. Appl. Crystallogr.* **2007**, *40* (4), 658–674. https://doi.org/10.1107/s0021889807021206.

(38) Adams, P. D.; Afonine, P. V.; Bunkóczi, G.; Chen, V. B.; Davis, I. W.; Echols, N.; Headd, J. J.; Hung, L.-W.; Kapral, G. J.; Grosse-Kunstleve, R. W.; McCoy, A. J.; Moriarty, N. W.; Oeffner, R.; Read, R. J.; Richardson, D. C.; Richardson, J. S.; Terwilliger, T. C.; Zwart, P. H. PHENIX: A Comprehensive Python-Based System for Macromolecular Structure Solution. *Acta*

Crystallogr. Sect. D: Biol. Crystallogr. **2010**, *66* (2), 213–221. https://doi.org/10.1107/s0907444909052925.

(39) Emsley, P.; Lohkamp, B.; Scott, W. G.; Cowtan, K. Features and Development of Coot. *Acta Crystallogr. Sect. D: Biol. Crystallogr.* **2010**, *66* (4), 486–501. https://doi.org/10.1107/s0907444910007493.

(40) Xiao, Z.; Wedd, A. G. The Challenges of Determining Metal– Protein Affinities. *Nat. Prod. Rep.* **2010**, *27* (5), 768–789. https://doi.org/10.1039/b906690j.

(41) Stoll, S.; Schweiger, A. EasySpin, a Comprehensive Software Package for Spectral Simulation and Analysis in EPR. *J. Magn. Reson.* **2006**, *178* (1), 42–55. https://doi.org/10.1016/j.jmr.2005.08.013.

(42) Diaz-Moreno, S.; Hayama, S.; Amboage, M.; Freeman, A.; Sutter, J.; Duller, G. I20; the Versatile X-Ray Absorption Spectroscopy Beamline at Diamond Light Source. *J. Phys.: Conf. Ser.* **2009**, *190* (1), 012038. https://doi.org/10.1088/1742-6596/190/1/012038.

(43) Hayama, S.; Duller, G.; Sutter, J. P.; Amboage, M.; Boada, R.; Freeman, A.; Keenan, L.; Nutter, B.; Cahill, L.; Leicester, P.; Kemp, B.; Rubies, N.; Diaz-Moreno, S. The Scanning Four-bounce Monochromator for Beamline I20 at the Diamond Light Source. *J. Synchrotron Radiat.* **2018**, *25* (5), 1556–1564. https://doi.org/10.1107/s1600577518008974.

(44) Ravel, B.; Newville, M. ATHENA, ARTEMIS, HEPHAESTUS: Data Analysis for X-ray Absorption Spectroscopy Using IFEFFIT. *J. Synchrotron Radiat.* **2005**, *12* (4), 537–541. https://doi.org/10.1107/s0909049505012719.

(45) Joseph, C.; DeBeer, S. *Cu K-Alpha HERFD-XANES of SmAA10A-Cu(I)*; 2024. https://doi.org/10.15151/ESRF-DC-1469091709 (accessed 2024-02-05).

(46) Mazurenko, I.; Hitaishi, V. P.; Lojou, E. Recent Advances in Surface Chemistry of Electrodes to Promote Direct Enzymatic Bioelectrocatalysis. *Curr. Opin. Electrochem.* **2020**, *19*, 113–121. https://doi.org/10.1016/j.coelec.2019.11.004.

(47) Hitaishi, V. P.; Clément, R.; Quattrocchi, L.; Parent, P.; Duché, D.; Zuily, L.; Ilbert, M.; Lojou, E.; Mazurenko, I. Interplay between Orientation at Electrodes and Copper Activation of Thermus Thermophilus Laccase for O2 Reduction. *J. Am. Chem. Soc.* **2020**, *142* (3), 1394–1405. https://doi.org/10.1021/jacs.9b11147.

(48) Neese, F. Software Update: The ORCA Program System, Version 4.0. *Wiley Interdiscip. Rev.: Comput. Mol. Sci.* **2018**, *8* (1). https://doi.org/10.1002/wcms.1327.

(49) Neese, F.; Wennmohs, F.; Becker, U.; Riplinger, C. The ORCA Quantum Chemistry Program Package. *J. Chem. Phys.* **2020**, *152* (22), 224108. https://doi.org/10.1063/5.0004608.

(50) Becke, A. Density-Functional Exchange-Energy Approximation with Correct Asymptotic Behavior. *Phys. Rev., A* **1988**, *38* (6), 3098–3100. https://doi.org/10.1103/physreva.38.3098.

(51) Perdew, J. Density-Functional Approximation for the Correlation Energy of the Inhomogeneous Electron Gas. *Phys. Rev., B Condens. Matter* **1986**, *33* (12), 8822–8824.

(52) Weigend, F.; Ahlrichs, R. Balanced Basis Sets of Split Valence, Triple Zeta Valence and Quadruple Zeta Valence Quality for H to Rn: Design and Assessment of Accuracy. *Phys Chem Chem Phys* **2005**, *7* (18), 3297–3299. https://doi.org/10.1039/b508541a.

(53) Weigend, F. Accurate Coulomb-Fitting Basis Sets for H to Rn. *Physical Chemistry Chemical Physics* **2006**, *8* (9), 1057–1065. https://doi.org/10.1039/b515623h.

(54) Gómez-Piñeiro, R. J.; Drosou, M.; Bertaina, S.; Decroos, C.; Simaan, A. J.; Pantazis, D. A.; Orio, M. Decoding the Ambiguous Electron Paramagnetic Resonance Signals in the Lytic

Polysaccharide Monooxygenase from Photorhabdus Luminescens. *Inorg. Chem.* **2022**, *61* (20), 8022–8035. https://doi.org/10.1021/acs.inorgchem.2c00766.

(55) Barone, V.; Cossi, M. Quantum Calculation of Molecular Energies and Energy Gradients in Solution by a Conductor Solvent Model. *J. Phys. Chem. A* **1998**, *102* (11), 1995–2001. https://doi.org/10.1021/jp9716997.

(56) Li, L.; Li, C.; Zhang, Z.; Alexov, E. On the Dielectric "Constant" of Proteins: Smooth Dielectric Function for Macromolecular Modeling and Its Implementation in DelPhi. *J. Chem. Theory Comput.* **2013**, *9* (4), 2126–2136. https://doi.org/10.1021/ct400065j.

(57) Ho, J. Are Thermodynamic Cycles Necessary for Continuum Solvent Calculation of p K a s and Reduction Potentials? *Phys. Chem. Chem. Phys.* **2014**, *17* (4), 2859–2868. https://doi.org/10.1039/c4cp04538f.

(58) Marenich, A. V.; Cramer, C. J.; Truhlar, D. G. Universal Solvation Model Based on Solute Electron Density and on a Continuum Model of the Solvent Defined by the Bulk Dielectric Constant and Atomic Surface Tensions. *J. Phys. Chem. B* **2009**, *113* (18), 6378–6396. https://doi.org/10.1021/jp810292n.

(59) Pavlishchuk, V. V.; Addison, A. W. Conversion Constants for Redox Potentials Measured versus Different Reference Electrodes in Acetonitrile Solutions at 25°C. *Inorg. Chim. Acta* **2000**, *298* (1), 97–102. https://doi.org/10.1016/s0020-1693(99)00407-7.

(60) Perdew, J. P.; Wang, Y. Accurate and Simple Analytic Representation of the Electron-Gas Correlation Energy. *Phys. Rev. B* **1992**, *45* (23), 13244–13249. https://doi.org/10.1103/physrevb.45.13244.

(61) Becke, A. D. Density-functional Thermochemistry. III. The Role of Exact Exchange. *The Journal of Chemical Physics* **1993**, *98* (7), 5648–5652. https://doi.org/10.1063/1.464913.

(62) Drosou, M.; Mitsopoulou, C. A.; Orio, M.; Pantazis, D. A. EPR Spectroscopy of Cu(II) Complexes: Prediction of g-Tensors Using Double-Hybrid Density Functional Theory. *Magnetochemistry* **2022**, *8* (4), 36. https://doi.org/10.3390/magnetochemistry8040036.

(63) Gómez-Piñeiro, R. J.; Pantazis, D. A.; Orio, M. Comparison of Density Functional and Correlated Wave Function Methods for the Prediction of Cu(II) Hyperfine Coupling Constants. *ChemPhysChem* **2020**, *21* (24), 2667–2679. https://doi.org/10.1002/cphc.202000649.

(64) Chong, D. P.; BARONE, V. Recent Advances in Density Functional Methods. *Recent Adv. Comput. Chem.* **1995**, 287–334. https://doi.org/10.1142/9789812830586_0008.

(65) Lee, C.; Yang, W.; Parr, R. G. Development of the Colle-Salvetti Correlation-Energy Formula into a Functional of the Electron Density. *Phys. Rev. B* **1988**, *37* (2), 785–789. https://doi.org/10.1103/physrevb.37.785.

(66) CASIDA, M. E. Time-Dependent Density Functional Response Theory for Molecules. In *Recent Advances in Density Functional Methods*; Recent Advances in Density Functional Methods; Recent Advances in Density Functional Methods, 2011; Vol. 1, pp 155–192. https://doi.org/10.1142/9789812830586_0005.

(67) Stratmann, R. E.; Scuseria, G. E.; Frisch, M. J. An Efficient Implementation of Time-Dependent Density-Functional Theory for the Calculation of Excitation Energies of Large Molecules. *The Journal of Chemical Physics* **1998**, *109* (19), 8218–8224. https://doi.org/10.1063/1.477483.

(68) Bauernschmitt, R.; Ahlrichs, R. Treatment of Electronic Excitations within the Adiabatic Approximation of Time Dependent Density Functional Theory. *Chem Phys Lett* **1996**, *256* (4–5), 454–464. https://doi.org/10.1016/0009-2614(96)00440-x.

(69) Hirata, S.; Head-Gordon, M. Time-Dependent Density Functional Theory for Radicals - An Improved Description of Excited States with Substantial Double Excitation Character. *Chem Phys Lett* **1999**, *302* (5–6), 375–382. https://doi.org/10.1016/s0009-2614(99)00137-2.

(70) Hirata, S.; Head-Gordon, M. Time-Dependent Density Functional Theory within the Tamm-Dancoff Approximation. *Chem Phys Lett* **1999**, *314* (3–4), 291–299.

(71) Neese, F. Prediction of Electron Paramagnetic Resonance g Values Using Coupled Perturbed Hartree–Fock and Kohn–Sham Theory. *The Journal of Chemical Physics* **2001**, *115* (24), 11080. https://doi.org/10.1063/1.1419058.

(72) Neese, F. Prediction of Molecular Properties and Molecular Spectroscopy with Density Functional Theory: From Fundamental Theory to Exchange-Coupling. *Coord. Chem. Rev.* **2009**, *253* (5–6), 526–563. https://doi.org/10.1016/j.ccr.2008.05.014.

(73) George, S. D.; Petrenko, T.; Neese, F. Time-Dependent Density Functional Calculations of Ligand K-Edge X-Ray Absorption Spectra. *Inorg. Chim. Acta* **2008**, *361* (4), 965–972. https://doi.org/10.1016/j.ica.2007.05.046.

(74) George, S. D.; Petrenko, T.; Neese, F. Prediction of Iron K-Edge Absorption Spectra Using Time-Dependent Density Functional Theory. *J. Phys. Chem. A* **2008**, *112* (50), 12936–12943. https://doi.org/10.1021/jp803174m.

(75) Yanai, T.; Tew, D. P.; Handy, N. C. A New Hybrid Exchange–Correlation Functional Using the Coulomb-Attenuating Method (CAM-B3LYP). *Chem. Phys. Lett.* **2004**, *393* (1–3), 51–57. https://doi.org/10.1016/j.cplett.2004.06.011.

(76) Lenthe, E. van; Snijders, J. G.; Baerends, E. J. The Zero-order Regular Approximation for Relativistic Effects: The Effect of Spin–Orbit Coupling in Closed Shell Molecules. *The Journal of Chemical Physics* **1996**, *105* (15), 6505–6516. https://doi.org/10.1063/1.472460.

(77) Pantazis, D. A.; Chen, X.-Y.; Landis, C. R.; Neese, F. All-Electron Scalar Relativistic Basis Sets for Third-Row Transition Metal Atoms. *J. Chem. Theory Comput.* **2008**, *4* (6), 908–919. https://doi.org/10.1021/ct800047t.

(78) Stoychev, G. L.; Auer, A. A.; Neese, F. Automatic Generation of Auxiliary Basis Sets. *J. Chem. Theory Comput.* **2017**, *13* (2), 554–562. https://doi.org/10.1021/acs.jctc.6b01041.

(79) Helmich-Paris, B.; Souza, B. de; Neese, F.; Izsák, R. An Improved Chain of Spheres for Exchange Algorithm. *J. Chem. Phys.* **2021**, *155* (10), 104109. https://doi.org/10.1063/5.0058766.

(80) Ciano, L.; Davies, G. J.; Tolman, W. B.; Walton, P. H. Bracing Copper for the Catalytic Oxidation of C–H Bonds. *Nat. Catal.* **2018**, *1* (8), 571–577. https://doi.org/10.1038/s41929-018-0110-9.

(81) Hemsworth, G. R.; Taylor, E. J.; Kim, R. Q.; Gregory, R. C.; Lewis, S. J.; Turkenburg, J. P.; Parkin, A.; Davies, G. J.; Walton, P. H. The Copper Active Site of CBM33 Polysaccharide Oxygenases. *J. Am. Chem. Soc.* **2013**, *135* (16), 6069–6077. https://doi.org/10.1021/ja402106e.

(82) Tandrup, T.; Muderspach, S. J.; Banerjee, S.; Santoni, G.; Ipsen, J. Ø.; Hernández-Rollán, C.; Nørholm, M. H. H.; Johansen, K. S.; Meilleur, F.; Leggio, L. L. Changes in Active-Site Geometry on X-Ray Photoreduction of a Lytic Polysaccharide Monooxygenase Active-Site Copper and Saccharide Binding. *IUCrJ* **2022**, *9* (Pt 5), 666–681. https://doi.org/10.1107/s2052252522007175.

(83) Zhang, L.; Koay, M.; Maher, M. J.; Xiao, Z.; Wedd, A. G. Intermolecular Transfer of Copper Ions from the CopC Protein of Pseudomonas Syringae. Crystal Structures of Fully Loaded CuICuII Forms. *J. Am. Chem. Soc.* **2006**, *128* (17), 5834–5850. https://doi.org/10.1021/ja058528x.

(84) Garribba, E.; Micera, G. The Determination of the Geometry of Cu(II) Complexes: An EPR Spectroscopy Experiment. *J. Chem. Educ.* **2006**, *83* (8), 1229. https://doi.org/10.1021/ed083p1229.

(85) Courtade, G.; Ciano, L.; Paradisi, A.; Lindley, P. J.; Forsberg, Z.; Sørlie, M.; Wimmer, R.; Davies, G. J.; Eijsink, V. G. H.; Walton, P. H.; Aachmann, F. L. Mechanistic Basis of Substrate–O2 Coupling within a Chitin-Active Lytic Polysaccharide Monooxygenase: An Integrated NMR/EPR Study. *Proc. Natl. Acad. Sci.* **2020**, *117* (32), 19178–19189. https://doi.org/10.1073/pnas.2004277117.

(86) Addison, A. W.; Rao, T. N.; Reedijk, J.; Rijn, J. van; Verschoor, G. C. Synthesis, Structure, and Spectroscopic Properties of Copper(II) Compounds Containing Nitrogen?Sulphur Donor Ligands; the Crystal and Molecular Structure of Aqua[1,7-Bis(N-Methylbenzimidazol-2?-Yl)-2,6-Dithiaheptane]Copper(II) Perchlorate. *J. Chem. Soc., Dalton Trans.* **1984**, No. 7, 1349–8. https://doi.org/10.1039/dt9840001349.

(87) Kau, L. S.; Spira-Solomon, D. J.; Penner-Hahn, J. E.; Hodgson, K. O.; Solomon, E. I. X-Ray Absorption Edge Determination of the Oxidation State and Coordination Number of Copper. Application to the Type 3 Site in Rhus Vernicifera Laccase and Its Reaction with Oxygen. *J. Am. Chem. Soc.* **1987**, *109* (21), 6433–6442. https://doi.org/10.1021/ja00255a032.

(88) Vu, V. V.; Beeson, W. T.; Span, E. A.; Farquhar, E. R.; Marletta, M. A. A Family of Starch-Active Polysaccharide Monooxygenases. *Proc. Natl. Acad. Sci.* **2014**, *111* (38), 13822–13827. https://doi.org/10.1073/pnas.1408090111.

(89) Garcia-Santamarina, S.; Probst, C.; Festa, R. A.; Ding, C.; Smith, A. D.; Conklin, S. E.; Brander, S.; Kinch, L. N.; Grishin, N. V.; Franz, K. J.; Riggs-Gelasco, P.; Leggio, L. L.; Johansen, K. S.; Thiele, D. J. A Lytic Polysaccharide Monooxygenase-like Protein Functions in Fungal

Copper Import and Meningitis. *Nat. Chem. Biol.* **2020**, *16* (3), 337–344. https://doi.org/10.1038/s41589-019-0437-9.

(90) Kjaergaard, C. H.; Qayyum, M. F.; Wong, S. D.; Xu, F.; Hemsworth, G. R.; Walton, D. J.; Young, N. A.; Davies, G. J.; Walton, P. H.; Johansen, K. S.; Hodgson, K. O.; Hedman, B.; Solomon, E. I. Spectroscopic and Computational Insight into the Activation of O2 by the Mononuclear Cu Center in Polysaccharide Monooxygenases. *Proc. Natl. Acad. Sci. U.S.A.* **2014**, *111* (24), 8797–8802. https://doi.org/10.1073/pnas.1408115111.

(91) Krause, M. O.; Oliver, J. H. Natural Widths of Atomic K and L Levels, K α X-Ray Lines and Several K L L Auger Lines. *J. Phys. Chem. Ref. Data* **1979**, *8* (2), 329–338. https://doi.org/10.1063/1.555595.

(92) Jeuken, L. J. C.; Armstrong, F. A. Electrochemical Origin of Hysteresis in the Electron-Transfer Reactions of Adsorbed Proteins: Contrasting Behavior of the “Blue” Copper Protein, Azurin, Adsorbed on Pyrolytic Graphite and Modified Gold Electrodes. *J. Phys. Chem. B* **2001**, *105* (22), 5271–5282. https://doi.org/10.1021/jp004283t.

(93) Roger, M.; Sciara, G.; Biaso, F.; Lojou, E.; Wang, X.; Bauzan, M.; Giudici-Orticoni, M.-T.; Vila, A. J.; Ilbert, M. Impact of Copper Ligand Mutations on a Cupredoxin with a Green Copper Center. *Biochim. Biophys. Acta (BBA) - Bioenerg.* **2017**, *1858* (5), 351–359. https://doi.org/10.1016/j.bbabio.2017.02.007.

(94) Zouraris, D.; Dimarogona, M.; Karnaouri, A.; Topakas, E.; Karantonis, A. Direct Electron Transfer of Lytic Polysaccharide Monooxygenases (LPMOs) and Determination of Their Formal Potentials by Large Amplitude Fourier Transform Alternating Current Cyclic Voltammetry. *Bioelectrochemistry* **2018**, *124*, 149–155. https://doi.org/10.1016/j.bioelechem.2018.07.009.

(95) Zouraris, D.; Karnaouri, A.; Xydou, R.; Topakas, E.; Karantonis, A. Exploitation of Enzymes for the Production of Biofuels: Electrochemical Determination of Kinetic Parameters of LPMOs. *Appl. Sci.* **2021**, *11* (11), 4715. https://doi.org/10.3390/app11114715.

(96) Cordas, C. M.; Valério, G. N.; Stepnov, A.; Kommedal, E.; Kjendseth, Å. R.; Forsberg, Z.; Eijsink, V. G. H.; Moura, J. J. G. Electrochemical Characterization of a Family AA10 LPMO and the Impact of Residues Shaping the Copper Site on Reactivity. *J. Inorg. Biochem.* **2023**, *238*, 112056. https://doi.org/10.1016/j.jinorgbio.2022.112056.

(97) Frandsen, K. E. H.; Simmons, T. J.; Dupree, P.; Poulsen, J.-C. N.; Hemsworth, G. R.; Ciano, L.; Johnston, E. M.; Tovborg, M.; Johansen, K. S.; Freiesleben, P. von; Marmuse, L.; Fort, S.; Cottaz, S.; Driguez, H.; Henrissat, B.; Lenfant, N.; Tuna, F.; Baldansuren, A.; Davies, G. J.; Leggio, L. L.; Walton, P. H. The Molecular Basis of Polysaccharide Cleavage by Lytic Polysaccharide Monooxygenases. *Nature Chemical Biology* **2016**, *12* (4), 298–303. https://doi.org/10.1038/nchembio.2029.

(98) Ciano, L.; Paradisi, A.; Hemsworth, G. R.; Tovborg, M.; Davies, G. J.; Walton, P. H. Insights from Semi-Oriented EPR Spectroscopy Studies into the Interaction of Lytic Polysaccharide Monooxygenases with Cellulose. *Dalton Trans.* **2020**, *49* (11), 3413–3422. https://doi.org/10.1039/c9dt04065j.

(99) Langerman, M.; Langevelde, P. H. van; Vijver, J. J. van de; Siegler, M. A.; Hetterscheid, D. G. H. Scaling Relation between the Reduction Potential of Copper Catalysts and the Turnover Frequency for the Oxygen and Hydrogen Peroxide Reduction Reactions. *Inorg. Chem.* **2023**, *62* (48), 19593–19602. https://doi.org/10.1021/acs.inorgchem.3c02939.

(100) Jones, S. M.; Transue, W. J.; Meier, K. K.; Kelemen, B.; Solomon, E. I. Kinetic Analysis of Amino Acid Radicals Formed in H2O2-Driven CuI LPMO Reoxidation Implicates Dominant

Homolytic Reactivity. *Proc National Acad Sci* **2020**, *117* (22), 11916–11922. https://doi.org/10.1073/pnas.1922499117.

(101) Bissaro, B.; Streit, B.; Isaksen, I.; Eijsink, V. G. H.; Beckham, G. T.; DuBois, J. L.; Røhr, Å. K. Molecular Mechanism of the Chitinolytic Peroxygenase Reaction. *Proc. Natl. Acad. Sci.* **2020**, *117* (3), 1504–1513. https://doi.org/10.1073/pnas.1904889117.

TOC Graphic and synopsis

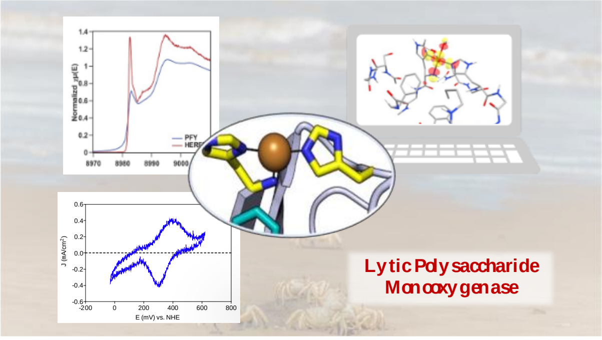

The physicochemical properties of the model bacterial Lytic Polysaccharide Monooxygenase (*Sm*AA10 or CBP21) were evaluated with a range of experimental tools combined with DFT calculations.